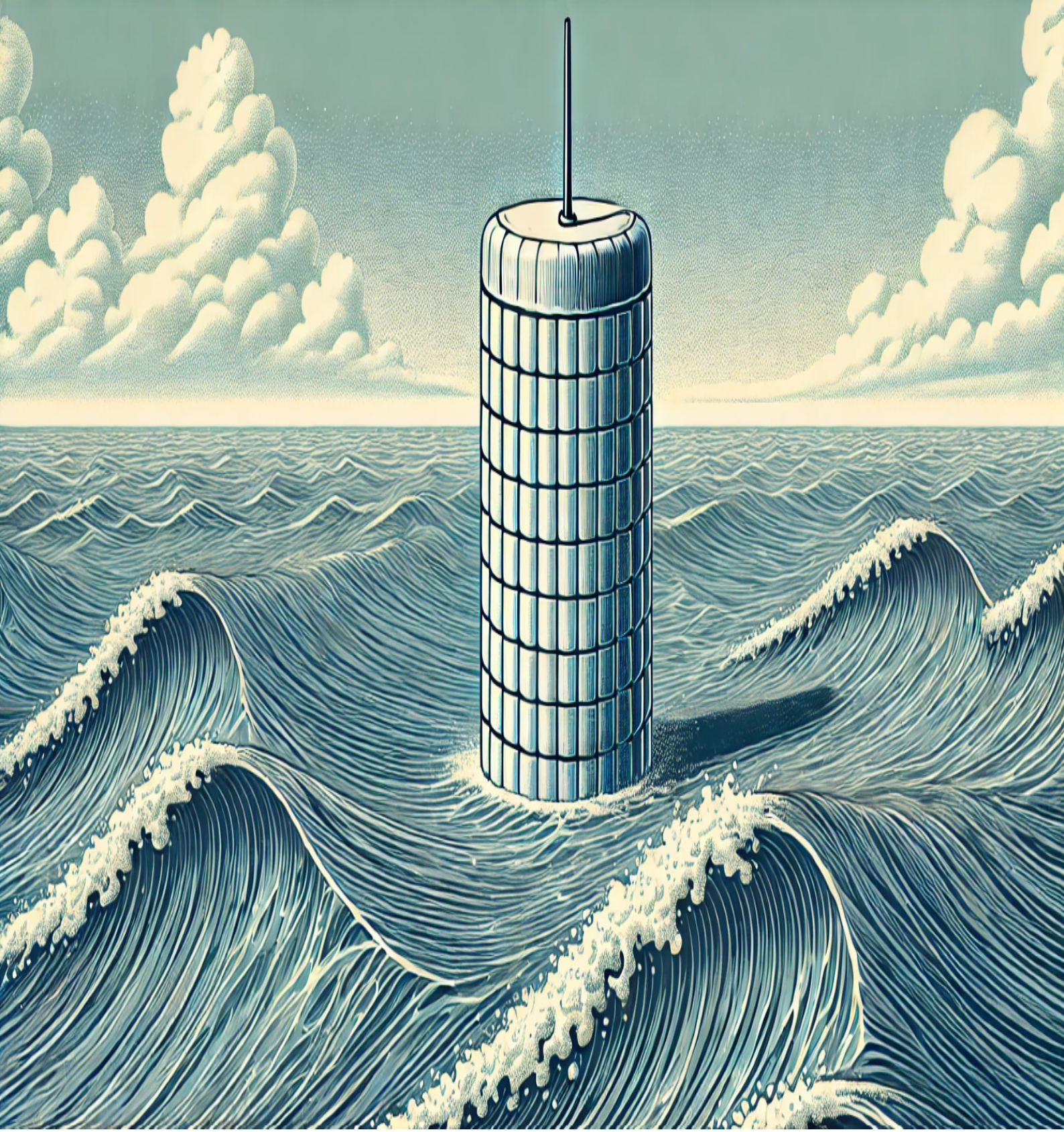

The Influence of Limiting Power Production on the Levelized Cost of Electricity in Wave Energy

Julie Borms

The Influence of Limiting Power Production on the Levelized Cost of Electricity in Wave Energy

Julie Borms

5102022
MSc Civil Engineering TU Delft

Supervised by
Dr. George Lavidas
Vaibhav Raghavan

To be defended on August 19th 2024
Faculty of Civil Engineering and Geosciences

Abstract

With the European Commission's ambitious goals for reducing greenhouse gas emissions and increasing renewable energy usage, marine renewables, including wave energy, have gained attention as a promising source of clean and predictable energy. Despite its potential, wave energy has lagged behind other renewable technologies like wind and solar, primarily due to higher costs and slower commercialization. This thesis investigates the impact of power output capping on the levelized cost of electricity (LCOE) of wave energy converters (WECs), a crucial metric for assessing their commercial viability. The research uses numerical modeling to calculate the theoretical LCOE/kg, considering both uncapped and capped power outputs.

Using a cylindrical point absorber WEC, the study employs a boundary element method (BEM) solver to model hydrodynamic parameters, such as response amplitude operators and excitation forces. By constructing power matrices, the research analyzes the effects of two capping strategies on the AEP and capacity factor in both medium and high energy regions.

Results indicate that capping significantly influences the LCOE, with small variations observed between medium- and high-energy regions. The study highlights that specifically PTO damping capping has the most negative economic implication, with similar changes in LCOE in terms of percentage observed in high-energy regions and medium-energy regions. These findings contribute to the broader goal of advancing the commercialization of wave energy, supporting the transition towards a more sustainable and climate-neutral energy future.

Preface

As my studies at Delft University of Technology draw to a close, I am grateful for the support and guidance I have received throughout this journey. First and foremost, I want to thank to Dr. George Lavidas. His passion for renewable energy has been a source of inspiration for me. His expertise and encouragement have spiked my interest in marine renewables and guided me through various challenges during this thesis. Due to his influence, I am excited to pursue a career within the renewable energy sector next year.

I would also like to express my deepest appreciation to my daily supervisor, Vaibhav Raghavan. His patience and guidance have been invaluable, especially in helping me understand the technical aspects of this research. Throughout the process, his support ensured I remained on the right track.

Finally, I am grateful to my family for their unwavering support and encouragement, especially during difficult times.

Julie Borms
July 2024, Delft

Contents

List of Figures

List of Tables

Nomenclature

∇p	Gradient of pressure
ν	Viscosity of the fluid
ω	Angular frequency
Φ	Velocity potential
Φ_D	Diffraction potential
Φ_I	Incident wave potential
Φ_R	Radiation potential
ρ	Water density
ζ	Free surface elevation
C_D	Morison's drag coefficient
F_e	Wave excitation force
F_r	Wave radiation force
F_{hs}	Hydrostatic force
F_{PTO}	Power take-off force
H_s	Significant wave height
P	Absorbed power
r	Discount rate
S_b	Wetted surface area
T	Wave period
T_p	Peak wave period
u	Velocity of fluid particles
A	Added mass matrix
B	Radiation damping matrix

C	Hydrostatic restoring matrix
c	Wave propagation speed
E	Energy
g	Acceleration due to gravity
H	Wave height
k	Wave number
L	Wavelength
M	Mass matrix

Introduction

Our planet is in desperate need for an energy transition, moving away from fossil fuels towards more sustainable sources of power. It is estimated that the energy sector accounts for more than three-quarters of total greenhouse gas emissions globally [1]. In order to make significant progress, renewable ways of generating energy should be utilized, offering solutions that are not only sustainable but also effective in reducing our carbon footprint. The European Commission has set goals to reduce greenhouse gas emissions in 2023 by at least 55% compared to 1990, while increasing the use of renewable energy to a minimum of 32%. A more long-term goal includes being the first climate-neutral continent by 2050, putting even more pressure on the renewable energy industry [2].

Marine renewable energy technologies have emerged as a promising and abundant source of clean energy, offering reliable and inexhaustible electricity. Marine renewable energy systems, including wave energy converters (WECs), harness the power of the ocean to generate electricity. Wave energy is not only sustainable but also reliable due to its abundant resource availability [3, 4]. Compared to wind energy, it is more concentrated and continuous, making it a promising contributor to a stable and clean energy supply [5].

However, despite its potential, the implementation and commercialization of WECs is currently not comparable to other renewables like wind and solar energy. The wave energy industry is at a relatively immature stage and although many WECs have been developed, a dominant technology has not yet come forward [6]. Although wave energy possesses some significant benefits over wind and solar energy, such as its larger energy density and better predictability, it seems that wind and solar energy converters experienced much more progress than WECs [7]. In 2014, it was estimated that wave power research was about 30 years behind compared to solar or wind energy. This led to an increase of 50% of papers published on the topic of wave energy [8, 9, 10]. How is it possible that despite all this research, wave energy is still not as commercialized as its marine renewable opponents?

To evaluate 'commercialization', a useful metric is the Levelized Cost Of Electricity (LCOE) for wave energy. This includes the combined capital expenditure (CAPEX), operational expenditure (OPEX) and annual energy production taking into account a discount factor and project lifespan.

1.1 Literature Review and Research Gap

Several studies have looked into the different aspects of Wave Energy Converter (WEC) power production estimates, as well as their Levelized Cost Of Electricity (LCOE).

Baca et al. (2022) examined the current and future trends in the wave energy industry's LCOE [11]. Their findings indicated that estimates for 2020 LCOE ranged from \$0.35/kWh to \$0.85/kWh, with an average of \$0.57/kWh. To elaborate on these values, a recent study by Guo (2023) [12] reviewed the LCOE of various WECs and explored potential cost-reduction strategies. The study found that the LCOE could reach \$0.30/kWh by 2033 under conservative assumptions and under more optimistic scenarios, this reduction could be achieved by 2029. This optimistic scenario assumes more efficient energy capture and conversion, accelerated cost reductions and steeper learning curves from previous projects. However, while the study extensively examined LCOE, it did not delve into the limitations of power output and their implications on LCOE reduction strategies.

De Andres et al. (2016) performed a case study investigating the optimum size of WECs for a 20 MW array, comparing smaller converters with lower mass and a smaller amount of converters with high individual power ratings [13]. A size-rating analysis is carried out for several European locations in order to research the dependence between site location and optimal WEC size-rating. Several metrics for a techno-economic assessment of marine energy converters, including LCOE, are compared in this work. However, numerical modelling of the power matrices is not included.

Tan et al. (2022) explored a size optimization method to enhance the techno-economic performance of WECs, while taking into account both buoy sizing and PTO sizing [14]. Their findings suggest that while PTO sizing has a limited effect on buoy size determination, it can reduce the LCOE by 24% to 31%. Although this research's objective is not to delve deeply into details of PTO sizing, the study did offer a theoretical preliminary model for LCOE estimation, based on percentages rather than exact numbers. This approach is beneficial for this research as well in order for the outcome to remain as general as possible.

A study by Rusu and Onea (2012) conducted a comprehensive review of various technologies used for wave energy extraction [15]. The key takeaways included a comprehensive review of WEC technologies, focusing on their mechanisms and operational principles. However, the study primarily focused on technology descriptions and performance evaluations without extensively exploring the economic implications, such as the LCOE.

Mérigaud et al. (2018) addressed the power production assessment for WECs, highlighting the challenges posed by the power matrix [16]. The study focused on overcoming technical hurdles to enhance power capture efficiency. Control strategies were proposed to optimize power production, yet the economic implications, especially regarding LCOE, were not the central focus of their investigation.

Babarit et al. (2012) aimed to estimate the mean annual power absorption of a selection of eight WECs with different working principles [17]. What is useful in this study is their approach of relating the power performance to mass and area, such as absorbed energy per characteristic mass $[kWh/kg]$, per characteristic surface area $[MWh/m^2]$ and per root mean square of Power Take Off (PTO) force $[kWh/N]$. Expressing these characteristics per mass offers a more objective comparison between the different WECs. Unfortunately, the research did not go into the economic evaluation of the considered

WEC.

Ahamed et al. (2020) provided a comprehensive overview of advancements in WECs based on PTO systems [18]. The study also discussed the advantages and challenges of the PTO systems but did not explore their impact on the LCOE for wave energy. Similarly, Shuang et al (2021) reviewed various working methods of PTO systems in WECs but lacked an in-depth analysis of their economic impacts on LCOE reduction [19].

Conversely, Guo et al. (2022) investigated the combined impact of power take-off capping and wave resource descriptions on the performance of WECs [20]. Their findings highlighted the importance of accurately describing wave resources and optimizing PTO systems. While offering insights into WEC performance enhancement, this study did not extensively explore the economic implications of the suggested improvements or their direct relation to reducing LCOE.

In conclusion, while there have been numerous advancements in the field of wave energy conversion, there is still a significant research gap in the analysis of the combined technical and economic aspects of power capping. Although different studies looked into PTO optimization and PTO force capping, the capping of power matrices based on their power output has not yet been introduced. In general, the reviewed studies either focused on technical functionalities or on LCOE, without integrating both aspects and without performing capping on power matrices, rather than PTO systems. Optimizations for PTO damping coefficients and certain locations have been performed before, but a more general approach to how capping influences the LCOE has not yet been discussed. Therefore, closing this research gap by examining how capping of wave power influences the LCOE, is crucial for advancing the commercialization of wave energy.

1.2 Research Objectives

This thesis aims to explore how capping the power output of WECs influences their LCOE. It will do so by computing the theoretical LCOE of WECs using numerical modelling. A general approach will be used by considering regular waves and a constant PTO damping coefficient. This approach avoids performing an optimization for a certain device or location, providing a more objective comparison between uncapped and capped power outputs. In order to delve deeper into the influence of power capping in wave energy, a comparison between a medium-energy region and a high-energy region will be made to substantiate the conclusion further. The most straightforward form of capping is putting a maximum to the power output of the WEC. Another type of capping that will be researched is putting a maximum to the PTO damping coefficient. Another option would be to limit the frequency range over which the WEC operates. The boundaries of this frequency range would be very dependent on the wave scatter diagram of a certain location. Since using this method would be more location-specific, it is less suitable for this research's objective to remain impartial regarding location-specific optimizations.

This leads to the following research question:

'What is the influence of limiting power production on the levelized cost of electricity in wave energy?'

The following sub-research questions need to be answered:

'How can numerical modelling be used to compute the theoretical annual energy production of WECs? What open-source software is most useful in this case?'

'How can the power take-off damping coefficient be calculated?'

'How can a power matrix be constructed from numerically calculated hydrodynamic parameters, such as excitation force, radiation damping, added mass and response amplitude operators, based on the WEC characteristics such as hull size, weight, PTO etc.?'

'How does capping influence the annual energy production of WECs and therefore the LCOE? Is there a large difference between power output capping and power take-off capping?'

Additionally, a comparison with a high energy region will be made to answer the following question:

'Does capping have a similar influence on the LCOE in medium and high energy regions?'

By exploring these factors, this thesis aims to contribute to the ongoing efforts to make wave energy a more economically viable source of renewable energy, thereby playing a crucial role in climate change mitigation and the transition towards a sustainable future.

1.3 Thesis Structure

Chapter 2 provides the theoretical background information used in this research. In Chapter 3, the numerical formulation and model set-up are elaborated upon. Chapter 4 shows the results of the numerical simulations, as well as the computed power matrix and AEP. In this chapter, two methods of capping are introduced. Chapter 5 consists of an economic model to estimate the LCOE. Chapter 6 draws a conclusion of the research project.

1.4 Wave Energy Converters

1.4.1 Types of WEC

Different concepts of WECs have been introduced so far. These can be categorized based on their operating principles into three main types: overtopping devices, oscillating water columns and oscillating bodies. Figure 1.1 provides an overview of the three main categories of WEC based on operating device [21]. In this section, those three main categories are discussed shortly.

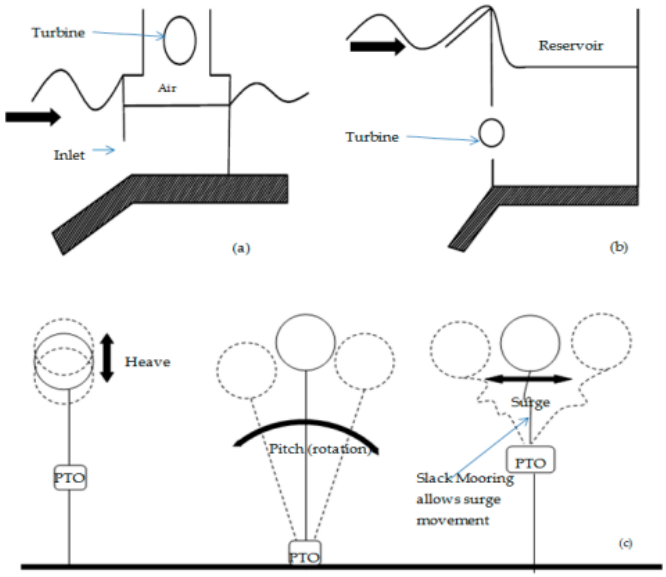

Figure 1.1: Oscillating water columns (a), overtopping devices (b) and oscillating bodies (c).

Oscillating Water Column

Figure 1.2: Integrated OWC power plant of Mutriku.

Figure 1.3: Offshore floating OWC Ocean Energy Buoy.

The oscillating water column (OWC) typically consists of a submerged structure with an air chamber. Incident waves would then cause fluctuations in air pressure in this cham-

ber. This reciprocating air is used to generate power. Usually, OWC devices are equipped with air turbines as power take-off systems that transform this air into mechanical power. An example of an air turbine is the Wells turbine, which is an axial flow self-rectifying turbine [22]. OWCs can be either floating or fixed, depending on the distance to shore. Some fixed OWCs are integrated into hydraulic structures like breakwaters, which offers easier accessibility for maintenance. An example is the Mutriku Wave Power Plant in Spain, which is integrated into the existing breakwater at the Mutriku harbour, see Figure 1.2 [23]. This power plant has a rated power of 300 kW. Conversely, offshore floating OWCs can harness more energy due to higher and more powerful waves in offshore environments. For this reason, floating OWCs are often more expensive since they have to be designed to withstand harsher wave and weather conditions. An example is the Ocean Energy Buoy, see Figure 1.3 [24]. This floating OWC has been used in different test sites, including Hawaii and Ireland. Its rated power is approximately 500 kW [25].

Oscillating Body

Figure 1.4: Point absorber CorPower C4 device.

Figure 1.5: Multi-body oscillating body Pelamis.

Oscillating bodies are WECs that oscillate in response to wave motions. These oscillations include translational motions (surge, sway and heave) as well as rotational motions (roll, pitch and yaw). Oscillating bodies have the ability to capture wave energy coming from different directions, making them particularly effective in more intense wave environments. Different concepts have been introduced, ranging from single-heaving bodies to complex multi-body configurations. The most straightforward example is the point absorber. This structure is relatively small compared to the wavelength and is attached to a mooring system when employed in offshore conditions. This configuration allows the device to capture wave energy from multiple directions as it moves vertically with the wave's motions. A power take-off system is activated through the vertical moments of the point absorber, which then operates a generator to convert mechanical energy into electrical energy. An example of a point absorber is the CorPower C4 device with a rated power of 300 kW [26], see Figure 1.4 [27]. CorPower C4 has been used on various test sides, including Sweden and Portugal. An example of a complex multi-body configuration oscillating body is Pelamis, which has, amongst others, been deployed in the European

Marine Energy Centre (EMEC) in Orkney, Scotland, see Figure 1.5 [28]. Pelamis has a rated power of 750 kW [25].

Overtopping Device

Overtopping devices harness wave energy by capturing the water from incoming waves into a reservoir. As the incident waves elevate the water, it is flushed into the reservoir. The potential energy of the trapped water is then transformed into mechanical energy using a turbine. This turbine is usually activated by the stored water that is released out of the reservoir into the ocean. The turbine essentially converts potential energy into mechanical energy, which is subsequently transformed into electrical energy. An example of an overtopping device in Denmark is Wave Dragon, see Figure 1.6 [29], which has a power rating of 20 kW [25].

Figure 1.6: Overtopping Device Wave Dragon.

1.5 Comparative Analysis of BEM Solvers for Wave-Structure Interactions

Numerical modeling is a critical tool for studying wave energy converters (WECs). These models allow researchers to predict WEC behavior under various ocean conditions, estimate the forces acting on them, and assess their power output. Among the different numerical methods, Boundary Element Methods (BEM) are particularly useful for conducting hydrodynamic analyses of WECs. This approach involves solving linear partial differential equations, as discussed in Sections 2.1 and 2.2.

In this section, three BEM solvers are compared: HAMS, NEMOH and WAMIT. Their features, advantages and limitations are explored, particularly in the context of constructing power matrices for point absorber WECs.

Table 1.1 provides a comparison of the main elements between HAMS, NEMOH and WAMIT.

	HAMS	**NEMOH**	**WAMIT**
Type	Open-source	Open-source	Commercial
Theory	Potential flow theory, Laplace equation, Newman's approximation	Potential flow theory, Laplace equation, interpolation methods	Potential flow theory, Laplace equation, Newman's approximation
User documentation	Limited	Moderate	Extensive, with detailed manuals and test cases
Green's function evaluation	Newman's approximation	Table of around 2,000,000 values	Newman's approximation
Computation time	3/4 amount of time as WAMIT	5 times as much time as WAMIT	Relatively fast
Multi-body interaction	No	Yes	Yes
Disadvantages	Fewer documentation	Irregular frequencies	Commercial use only

Table 1.1: Overview of comparison between HAMS, NEMOH and WAMIT.

To address the sub-research question *'How can numerical modelling be used to compute the theoretical annual energy production of WECs? What open-source software is most useful in this case?'*, this section presents a comparative analysis of three BEM solvers: HAMS, NEMOH and WAMIT.

Both HAMS and WAMIT employ advanced numerical techniques, such as Newman's approximation for solving Green's function and the strategic use of symmetrical properties to enhance computational efficiency. Additionally, HAMS leverages OpenMP parallelization techniques, which significantly reduce computational efforts while maintaining accuracy. This efficiency is particularly beneficial for managing complex scenarios in WEC analysis.

The open-source nature of HAMS supports academic research. This enhances its potential for further development in the future. In contrast, WAMIT's commercial constraints may limit accessibility due to licensing costs.

A final comparison shows that HAMS is a balanced option between NEMOH's challenges with irregular frequencies and WAMIT's commercial nature. HAMS delivers accurate hydrodynamic analysis while remaining user-friendly. Given its more recent introduction, HAMS presents an interesting option to further explore its potential. Therefore, HAMS will be the final choice for providing hydrodynamic coefficients to construct power matrices in this research.

Theoretical Background

In this chapter, the theoretical background of most boundary element method (BEM) solvers based on numerical simulations will be presented. The linear potential flow theory will be discussed in more detail in order to form a deeper understanding of the working principle of the BEM solver HAMS used in this research.

BEM is preferred over the finite element method or finite difference method because it efficiently handles domains by only discretizing boundaries on the body's surface, which reduces the computational cost. Additionally, BEM provides high accuracy in representing complex boundary conditions and is particularly effective for linear potential flow problems [30, 31].

2.1 The Linear Potential Flow Theory

In order to understand a fluid-structure interaction problem, two fundamental sets of equations in fluid dynamics need to be explained. The first is the continuity equation, which ensures the conservation of mass. The second consists of the Navier-Stokes equations, which describe the conservation of momentum.

2.1.1 Conservation of Mass: Continuity

The conservation of mass principle states that the mass of fluid entering a control volume must equal the mass of fluid leaving the control volume plus any change in mass over time. This principle states that mass cannot be created or destroyed within the system. The fluid is assumed to be incompressible, with a constant density. The incompressibility assumption allows for the conservation of volume. This means that the volume of fluid entering the control volume must equal the volume of fluid leaving the control volume since the fluid's density remains constant. Therefore, for incompressible fluids, both mass and volume are conserved. This allows writing the continuity equation, see Equation 2.1.

$$\vec{\nabla} \cdot \vec{u} = 0 \tag{2.1}$$

where $\vec{\mathbf{u}}$ represents the fluid velocity field.

2.1.2 Conservation of Momentum

Within a fluid domain, flow patterns can be described using the Navier-Stokes equations. The Navier-Stokes equations are derived from Newton's second law applied to fluid motion, expressing the conservation of momentum and making use of the conservation of mass principle. They describe how the velocity field of a fluid evolves due to various forces acting on a fluid element, including pressure, viscous and external forces. For an incompressible fluid, Equation 2.2 describes the conservation of momentum.

$$\frac{\partial \vec{u}}{\partial t} + (\vec{u} \cdot \nabla)\vec{u} = -\frac{1}{\rho}\nabla p + \nu \nabla^2 \vec{u} + F_b \tag{2.2}$$

where ρ is the density, p represents the pressure and ν is the viscosity of the fluid and F_b represents external body forces. The left-hand side of the equation represents the inertial forces, including local acceleration $\frac{\partial \vec{u}}{\partial t}$ and convective acceleration $(\vec{u} \cdot \nabla)\vec{u}$. The right-hand side includes the pressure gradient force $-\frac{1}{\rho}\nabla p$ and viscous forces $\nu \nabla^2 \vec{u}$.

2.1.3 Potential Flow

When introducing the potential flow theory, the flow of fluid particles has to be considered irrotational and non-viscous. Using these assumptions, a velocity potential can be introduced, see Equation 2.3.

$$\vec{u} = \nabla \Phi \tag{2.3}$$

$$\frac{\partial \Phi}{\partial x} = u, \quad \frac{\partial \Phi}{\partial y} = v, \quad \frac{\partial \Phi}{\partial z} = w \tag{2.4}$$

When looking at a fluid-structure interaction problem, Φ can be split into three different components:

$$\Phi = \Phi_R + \Phi_S + \Phi_I \tag{2.5}$$

where:

- Φ_R is the radiation potential from the oscillatory motion of the body in still water.
- Φ_S is the scattered potential caused by the scattering of waves.
- Φ_I is the incident undisturbed wave potential.

When considering harmonic waves, the solution to this linear problem in the time domain can be found in Equation 2.6 where $\hat{\Phi}$ is the complex amplitude of the total velocity potential and ω is the angular frequency.

$$\Phi = \mathrm{Re}\left\{\hat{\Phi} e^{i\omega t}\right\} \tag{2.6}$$

The first-order motions of the structure in a fluid are assumed to oscillate in a harmonic motion, resulting in the radiation potential. Because rigid bodies have six degrees of motion, this radiation potential is the sum of the six modes of motion from a wave-structure interaction. The radiation potential can then be described by Equation 2.7.

$$\hat{\Phi}_R = i\omega \sum_{j=1}^{6} \xi_j \hat{\Phi}_j, \quad j = 1, 2, \ldots, 6 \tag{2.7}$$

where ξ_j is the amplitude of motions, $\hat{\Phi}_j$ is the potential component from one degree of freedom. When considering the structure to be stationary, the scattered potential results from the scattering of the incoming waves on the structure.

To accurately describe the incident wave potential, it is essential to define the coordinate system used, see Figure 2.1 [32]. The incident wave is assumed to propagate at an angle β relative to the x-axis.

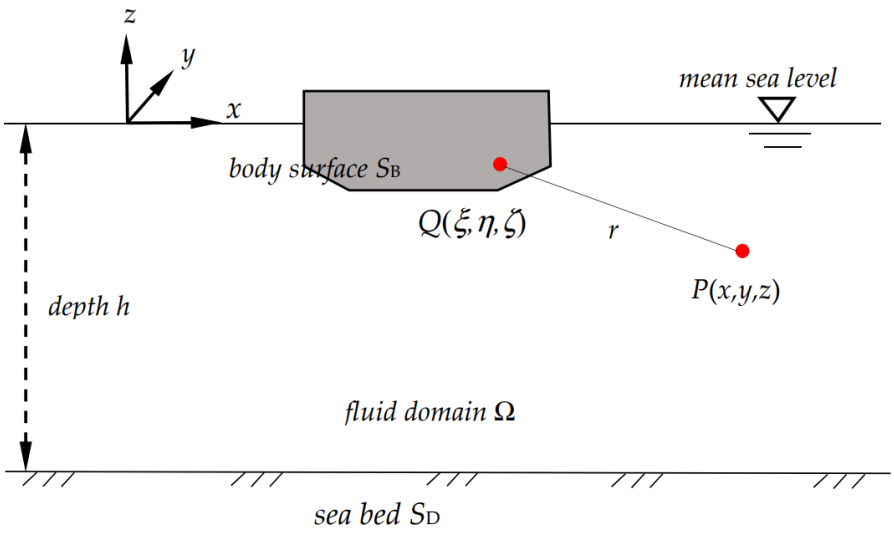

Figure 2.1: Definition of the coordinate system in the three-dimensional space employed by HAMS.

The incident undisturbed wave potential can be expressed in different forms depending on the water depth. The equations employed by the HAMS can be seen in Equations 2.8 and 2.9 for a finite and infinite depth respectively [32].

$$\hat{\Phi}_I = -\frac{igA}{\omega}\frac{\cosh(k(z+h))}{\cosh(kh)}e^{ik(x\cos\beta+y\sin\beta)}, \tag{2.8}$$

$$\hat{\Phi}_I = -\frac{igA}{\omega}e^{vz}e^{-iv(x\cos\beta+y\sin\beta)}, \tag{2.9}$$

where ω represents the angular frequency, g is the gravitational constant, k represents the wave number, h is the water depth relative to the fluid's surface and β is the angle of wave propagation relative to the x-axis.

For regular waves, the solution to the velocity potentials can be found by solving the Laplace equation (Equation 2.10) with appropriate boundary conditions. The Laplace equation results from combining Equations 2.1 and 2.3.

$$\nabla^2\hat{\Phi} = 0 \tag{2.10}$$

The following boundary conditions are taken into account:

- **Impermeability at the seabed**

$$\frac{\partial\hat{\Phi}}{\partial z} = 0, \quad \text{at } z = -h \tag{2.11}$$

$$\lim_{z\to\infty}\left(\frac{\partial\hat{\Phi}}{\partial z}\right) = 0 \tag{2.12}$$

- **Impermeability on the body's surface.** The velocity of the flow in the direction normal to the hull must be equal to the velocity of the hull itself in that same direction.

$$\frac{\partial\hat{\Phi}}{\partial n} = \hat{v}_n, \quad \text{at } S_b \tag{2.13}$$

- **Linearized free surface boundary condition.** When a fluid particle is on the free surface, it will stay there.

$$g\frac{\partial\hat{\Phi}}{\partial z} - \omega^2\hat{\Phi} = 0, \quad \text{at } z = 0 \tag{2.14}$$

- **Radiation wave condition.** Relatively far away from the floating body, no disturbances are felt due to the body's presence. R is the radial distance from the body.

$$\lim_{R\to\infty}\left[\sqrt{\frac{\omega^2}{g}R}\left(\frac{\partial\phi}{\partial R} - i\frac{\omega^2}{g}\phi\right)\right] = 0 \tag{2.15}$$

Combining the velocity potential with the Navier-Stokes equations, results in the linearized Bernoulli pressure equation (Equation 2.16). In this equation, the first-order fluctuating pressure induced by the incident waves is represented by the first term. The second term represents the hydrostatic pressure. A non-linear term $-\frac{1}{2}(\nabla\Phi)^2$ accounts for second-order wave drift but is neglected in this case due to the assumption of a relatively small flow velocity.

$$p = -\rho\frac{\partial\Phi}{\partial t} - \rho g z \tag{2.16}$$

Using the equations and assumptions above, the velocity components and pressure distribution of the potential flow solutions for gravity waves are shown in Equations 2.17, 2.18 and 2.19.

$$u(x,z,t) = \frac{\partial\hat{\Phi}}{\partial x} = \omega\zeta_a\frac{\cosh k(h+z)}{\sinh kh}\cos(kx-\omega t) \tag{2.17}$$

$$w(x,z,t) = \frac{\partial\hat{\Phi}}{\partial z} = \omega\zeta_a\frac{\sinh k(h+z)}{\sinh kh}\sin(kx-\omega t) \tag{2.18}$$

$$p(x,z,t) = \rho g\zeta_a\frac{\cosh k(h+z)}{\cosh kh}\cos(kx-\omega t) - \rho g z \tag{2.19}$$

where ζ_a is the amplitude of the free surface elevation with respect to z = 0, as defined in Equation 2.20.

$$\zeta(x,t) = \zeta_a\cos(kx-\omega t) \tag{2.20}$$

2.1.4 Green's Function

A Green's function is a solution to differential equations subject to boundary conditions. Within the context of BEM, it transforms the partial differential equations into an integral equations over the boundary of the body's surface using the boundary integral equation (BIE).

In BEM, there are two main formulations for solving BIEs: the source formulation and the potential formulation. In the source formulation, the BIE is expressed in terms of source strengths distributed over the body's surface. A source is a point on the surface where fluid flows radially outward, whereas at a sink fluid flows inward. A dipole is a combination of a source and a sink. The boundary integral equation must be solved for the unknown source strength or dipole moment. In the potential formulation, the velocity potential and its normal derivative on the boundary surface are solved for directly. This approach typically involves fewer unknowns compared to the source formulation but can be more complex to implement.

HAMS employs the source formulation, utilizing sources and dipoles to calculate the velocity potentials. This method is particularly effective for problems involving complex geometries and boundary conditions.

The full boundary integral equation satisfied by the radiation and scattered potentials on the body boundary takes the form of Equation 2.21 [32].

$$2\pi\hat{\Phi}_k(x) + \iint_{S_B} \hat{\Phi}_k(x)\frac{\partial G(x,x_s)}{\partial n_{x_s}}dS_{x_s} = \iint_{S_B} v_{n,k}(\vec{x_s})G(x,x_s)dS_{x_s}, \quad (k=1,2,\ldots,7), \tag{2.21}$$

where $\vec{x}$ is the field point, $\vec{x_s}$ denotes the source point, $\hat{\Phi}$ is the complex amplitude of the velocity potential, $G(\vec{x},\vec{x_s})$ is the Green's function representing the flow at $\vec{x}$ due to a source at $\vec{x_s}$, S_b is the wetted surface and $v_{n,k}$ denotes the k-th component of the body surface boundary condition. Subjects k = 1 to 6 refer to the six components of the radiated waves and subject k = 7 refers to the scattered waves.

When employing the lower-order panel method, the boundary surfaces are discretized into plane panels to approximate the exact geometry. The radiation and diffraction velocity potentials are represented by constant functions over each panel as well. Using this approach, the boundary integral equations (Equation 2.21) are discretized into Equation 2.22 [32].

$$2\pi\hat{\Phi}_k(x_i) + \sum_{j=1}^{N_p} D_{ij}\hat{\Phi}_k(x_j) = \sum_{j=1}^{N_p} S_{ij}V_{n,k}(x_j), \quad (i=1,2,\ldots,N_p; k=1,2,\ldots,7), \tag{2.22}$$

where N_p is the number of panels. The integrations of sources and dipoles over each panel are represented by Equations 2.23 and 2.24 respectively [32].

$$S_{ij} = \iint_{S_{B,j}} G(x_i,x_s)dS_{x_s} \tag{2.23}$$

$$D_{ij} = \iint_{S_{B,j}} \frac{\partial G(x_i,x_s)}{\partial n_{x_s}}dS_{x_s} \tag{2.24}$$

where $S_{B,j}$ denotes the j-th panel surface.

2.2 Equations of Motion

The equations of motion for the fluid-structure interaction problem can be expressed using Newton's second law that states that the net force equals mass times acceleration. In the time-domain, the motion of a rigid body can then be described through Equation 2.25.

$$M\ddot{x}(t) = F_{\text{hs}}(t) + F_{\text{e}}(t) + F_{\text{r}}(t) + F_{\text{pto}}(t) \tag{2.25}$$

where M represents the mass of the oscillating body, $\ddot{x}$ is the acceleration, F_{hs} represents the hydrostatic force, F_{e} is the excitation force, F_{r} represents the radiation force and F_{pto} is the PTO force.

Using potential flow theory as explained in Section 2.1, the forces in Equation 2.25 can be written as functions of the velocity potential:

$$F = \int_{S_b} \rho \frac{\partial \Phi}{\partial t} n \, dS_b \tag{2.26}$$

where ρ is the fluid density, n represents the unit vector normal to the body's surface and S_b is the wetted surface area.

As stated before, the motions of the waves and the device are assumed to be harmonic. Following this assumption, the terms in Equation 2.25 can be expressed in their spatial and temporal dependencies. The displacement, velocity and acceleration can then be described as shown in Equations 2.27, 2.28 and 2.29 respectively [33].

$$x(t) = \text{Re}\left\{\hat{\zeta}(\omega)e^{i\omega t}\right\} \tag{2.27}$$

$$\dot{x}(t) = \text{Re}\left\{i\omega\hat{\zeta}(\omega)e^{i\omega t}\right\} \tag{2.28}$$

$$\ddot{x}(t) = \text{Re}\left\{-\omega^2\hat{\zeta}(\omega)e^{i\omega t}\right\} \tag{2.29}$$

The next sections will describe each force in the frequency domain separately.

2.2.1 Hydrostatic Restoring Force

In undisturbed conditions, the hydrostatic force can be derived by integrating the hydrostatic pressure over the body's wetted surface. When the amplitudes of the body's motions are small, the linearization of the hydrostatic force provides a reasonably accurate approximation. In this case, the hydrostatic force becomes proportional to the displacement. The complex amplitude can then be written as shown in Equation 2.30 [33].

$$\hat{F}_{\mathrm{hs}} = -C\hat{\zeta} \tag{2.30}$$

where C is the hydrostatic coefficient. Since this research looks at a heaving point absorber, C is equal to $\rho g S_w$, where S_w is the cross-sectional area of the body at the waterline.

2.2.2 Excitation Force

The excitation force consists of two separate forces namely, the Froude-Krylov force F_{FK} and the scattered force F_{S} [33]. The Froude-Krylov force is derived from the incident undisturbed wave potential Φ_{I} and the scattered force is a result of the scattering potential Φ_{S}.

$$\hat{F}_{\mathrm{e}}(\omega) = \hat{F}_{\mathrm{FK}}(\omega) + \hat{F}_{\mathrm{S}}(\omega) \tag{2.31}$$

$$\hat{F}_{\mathrm{e}}(\omega) = i\omega\rho \left(\int_{S_{\mathrm{b}}} \left(\hat{\Phi}_{\mathrm{I}} \cdot n \right) \, dS_{\mathrm{b}} + \int_{S_{\mathrm{b}}} \left(\hat{\Phi}_{\mathrm{S}} \cdot n \right) \, dS_{\mathrm{b}} \right) \tag{2.32}$$

2.2.3 Radiation Force

The radiation force in heave can be obtained by integrating the radiation potential, as defined in Section 2.1.

$$F_r = -\omega^2 \rho \int_{S_b} \hat{\xi} \hat{\Phi}_R n dS_b \tag{2.33}$$

In the time-domain, the radiation force can be written as shown in Equation 2.34.

$$F_r(t) = -A_{33}(\omega)\ddot{x} - B_{33}(\omega)\dot{x} \tag{2.34}$$

where A is the added mass matrix and B is the damping matrix. Combining this with Equations 2.28 and 2.29, the amplitude of the radiation force in the frequency domain can be written as shown in Equation 2.35.

$$\hat{F}_r(\omega) = \omega^2 A_{33}(\omega)\hat{\zeta} - i\omega B_{33}(\omega)\hat{\zeta} \tag{2.35}$$

2.2.4 Power Take-Off Force

Typically, the reaction forces acting on a WEC consist the loads from the mooring system and the loads caused by the PTO equipment. In this research, the loads caused by the mooring system will be disregarded. Generally, the PTO system's control strategy introduces complex nonlinear dynamic behaviour. Within the frequency domain, the PTO reaction force must be linearized in order for the RAOs to be solved. In its linear form, the PTO force is composed of two contributions: the first one, which is proportional to velocity, represents a damper and the second one, which is proportional to the displacement of the body, is represented by a spring [33]. In this research, the PTO spring constant is disregarded.

$$\hat{F}_{\text{pto}} = -i\omega B_{\text{pto}}\hat{\zeta} \tag{2.36}$$

For the construction of power matrices, a constant PTO damping coefficient that is optimized for a specific frequency will be used. Section 2.3 provides a more in-depth analysis of the linearization process and the optimization of the PTO damping.

2.2.5 Equations of Motion in the Time- and Frequency-Domain

Taking into account all forces as described before, the final EOM is shown in Equation 2.37 in the time-domain for heave only.

$$(M_{33} + A_{33})\ddot{x} + B_{33}\dot{x} + C_{33}x = F_{\text{ext}} \tag{2.37}$$

where M_{33} is the mass in heave, A_{33} is the frequency-dependent added mass in heave, B is the total damping in heave and C_{33} is the hydrostatic restoring coefficient in heave. This equation can be transformed to the frequency domain by using Equations 2.27 to 2.29.

$$[-\omega^2(M_{33} + A_{33}(\omega)) + i\omega B_{33}(\omega) + C_{33}]\hat{\zeta} = F_{ext}(\omega) \tag{2.38}$$

Since this research is only looking at heave, the following notation will be used from now on for simplicity:

$$[-\omega^2(m + m_a(\omega)) + i\omega b(\omega) + c_h]\hat{\zeta} = f_{ext}(\omega) \tag{2.39}$$

where m is the mass of the system, m_a is the frequency-dependent added mass in heave, b is the frequency-dependent full damping in heave, c_h is the hydrostatic restoring coefficient as described in Section 2.2.1 and f_exti is the frequency-dependent excitation force in heave.

2.3 Optimal Power Take-Off Damping

Damping forces significantly affect the motion of offshore structures. Numerical tools, such as HAMS, can estimate potential damping forces, as discussed in Section 2.2. However, these models face challenges in fully capturing the impact of viscous damping forces due to their nonlinear nature. This section explains a method to calculate these viscous terms.

When looking at the equation of motion in Equation 2.40, b is said to be the full damping coefficient. This damping coefficient can be further split up into three components.

$$(m + m_a)\ddot{x} + b\dot{x} + c_h x = f_{\text{ext}} \tag{2.40}$$

$$b = b_a + b_{pto} + b_v \tag{2.41}$$

where b_a is the radiation damping heaving hydrodynamic coefficient, b_{pto} is the device-specific power take-off coefficient and b_v is the linearized viscous damping coefficient. Section 2.3.1 will discuss the radiation and viscous damping. The power take-off damping coefficient will be further elaborated upon in Section 2.3.2.

2.3.1 Linearized Viscous Damping Coefficient

As can be seen from the general EOM for a floating unit in heave in Equation 2.42, the viscous damping is a form of nonlinear damping.

$$(m + m_a)\ddot{x} + b_a\dot{x} + b_1|\dot{x}|\dot{x} + c_h x = f_{\text{ext}} \tag{2.42}$$

where m is the mass in heave, m_a is the added mass in heave, b_a is the radiation damping in heave and b_1 is the nonlinear damping coefficient related to the viscous damping.

In order to be able to solve the EOM, the nonlinear viscous term in Equation 2.42 needs to be linearized. Malta et al. (2010) [34] presented different methods to evaluate the damping coefficients based on free oscillation tests. Their study showed that the quadratic equation is appropriate to represent the viscous damping forces. In order to evaluate b_1, the linearization of the term $|\dot{x}|\dot{x}$ is performed using Lorentz' Linearization for a monochromatic wave [35, 36, 37].

$$|\dot{x}|\dot{x} = \frac{8}{3\pi} C_D \omega a \dot{x} \tag{2.43}$$

where a is the frequency-dependent amplitude of the WEC and C_D is Morison's drag coefficient. A drag coefficient of 0.30 is chosen for this research, based on the drag coefficient for CorPower C4 device due to its comparable dimensions and deployment locations [38, 39].

Equation 2.43 allows writing Equation 2.42 as follows:

$$(m + m_a)\ddot{x} + (b_a + \frac{8b_1}{3\pi} C_D \omega a)\dot{x} + c_h x = f_{\text{ext}} \tag{2.44}$$

which is a linearized equation with respect to time. When obtaining the RAOs (see Section 2.4), an iterative process is needed in order for the amplitudes a to match the RAOs. This is done by first assuming a value for the amplitude a and then iterating these assumed values until they match the RAOs. It can be assumed that the nonlinear damping term may be represented by the Morison equation drag term [40].

$$b_1 = \frac{1}{2}\rho A C_D \tag{2.45}$$

where A is the projected area of the vessel in the direction of the flow.

2.3.2 Power Take-Off Coefficient

The power take-off damping coefficient of a WEC significantly influences the dynamic response of the converter and the overall energy capture efficiency. An optimally chosen damping coefficient maximizes energy capture and aligns the system's natural frequency with prevalent wave frequencies, enhancing the resonance effect and overall system performance. Hals et al [41] proposed sub-optimal passive control including viscous losses for the PTO damping coefficient, as can be seen from Equation 2.46:

$$b_{\mathrm{PTO}}(\omega) = \sqrt{R_i(\omega)^2 + X_i(\omega)^2} \tag{2.46}$$

where

$$R_i(\omega) = b_a(\omega) + R_f \tag{2.47}$$

$$X_i(\omega) = i\omega(m_d + m_a(\omega)) + \left(\frac{c_h}{i\omega}\right) \tag{2.48}$$

R_i and X_i refer to the real and imaginary part of the intrinsic impedance of the heaving body, with R_f accounting for the viscous losses. The viscous damping has already been estimated in Section 2.3.1. This allows writing R_i as:

$$R_i(\omega) = b_a(\omega) + b_v(\omega) \tag{2.49}$$

As stated before, a frequency-optimized constant b_{pto} damping coefficient will be selected. This is done to avoid optimizations for each frequency, keeping in mind this research's objective to remain impartial regarding optimizations for specific locations or wave conditions. The final value will be based on the wave occurrence probability matrix. The WEC has to be able to capture energy at sea states with peak periods relevant to the location. Additionally, Ma et al. [42] found that using the optimized PTO damping coefficient at a wave period of 1.5-2.0 times the natural wave period of the undamped system resulted in a broader effective wave range.

2.4 Response Amplitude Operators

Finally, the Response Amplitude Operators (RAO's) can be calculated from the EOM in heave directly:

$$[(-m + m_a(\omega))\omega^2 - i\omega(b_a(\omega) + b_{pto} + b_v(\omega)) + c_h]\hat{\xi} = f_e(\omega) \tag{2.50}$$

where m and m_a are mass and frequency-dependent added mass, b_a is the frequency-dependent radiation damping, b_{PTO} is (constant) PTO damping coefficient and c_h is the hydrostatic restoring coefficient. This expression can be further simplified as:

$$C\xi = f_{\text{ext}} \quad \text{with } C = -\omega^2 (m + m_a) + i\omega(b_a + b_{pto} + b_v) + c_h \tag{2.51}$$

Using this form, the response amplitude operators can be calculated. The displacement in heave is:

$$x = \left[C^{-1}\right] f_e \tag{2.52}$$

Finally, the non-dimensional response amplitude operator (RAO) is derived:

$$Z_j(\omega, \beta) = \frac{\xi_j}{A} \tag{2.53}$$

where A is the amplitude of the incoming wave.

2.5 Energy and Power

The potential flow theory, as described in Section 2.1.3, can be employed to quantify the amount of potential energy that can be harnessed from sea waves. The total energy per wave cycle per unit surface area within the water column is given by Equation 2.54.

$$E_{\text{total}} = E_{\text{kinetic}} + E_{\text{potential}} = \frac{1}{4}\rho g\zeta_a^2 + \frac{1}{4}\rho g\zeta_a^2 = \frac{1}{2}\rho g\zeta_a^2 = \frac{1}{8}\rho g H^2 \tag{2.54}$$

where ρ is the water density, g is the acceleration due to gravity, ζ_a is the wave amplitude, and H is the wave height.

Using linear wave theory, the wave number k can be derived from the dispersion relation:

$$\omega^2 = gk\tanh(kh) \tag{2.55}$$

where h is the water depth, and ω is the angular wave frequency.

The wave propagation speed c, wavelength L and wave period T are respectively given by:

$$c = \frac{\omega}{k} \tag{2.56}$$

$$L = \frac{2\pi}{k} \tag{2.57}$$

$$T = \frac{2\pi}{\omega} \tag{2.58}$$

To estimate the power transfer over one wave cycle, the group speed c_g is essential:

$$c_g = cn \tag{2.59}$$

$$n = \frac{1}{2}\left(1 + \frac{2kh}{\sinh(2kh)}\right) \tag{2.60}$$

Using the equations above, the average available power for regular waves is defined in Equation 2.61.

$$\overline{P_w} = E_{\text{total}} c_g \tag{2.61}$$

In regular waves, the average absorbed power is directly proportional to the incident wave period and wave height. The absorbed power in regular waves can be calculated using Equation 2.62.

$$P = \frac{1}{2}(\frac{2\pi}{T})^2 b_{PTO}(\zeta\frac{H}{2})^2 \tag{2.62}$$

where b_{pto} is the frequency-dependent PTO damping, ζ are the frequency-dependent RAOs and T and H are the incident wave period and wave height respectively. Equation 2.62 is used to calculate the absorbed power for each sea state in the power matrix.

Methodology and Model Set-Up

In this chapter, the methodology used to conduct this research will be explained. The pre-processing of the required input for HAMS is elaborated upon as well.

3.1 Methodology

Before being able to run HAMS, a mesh file of the geometry of the WEC is needed. A cylindrical heaving point absorber will be used in this research. The geometry model of this cylinder is built using the Rhinoceros modelling software. Rhinoceros allows its users to define the amount of vertical and horizontal panels used in the cylinder, which is very useful for the conduction of a convergence study. Once the geometry model is made, it can be exported into a mesh format suitable for HAMS using BEMRosetta [43]. HAMS is able to determine the mass and hydrostatic restoring matrices. Since this study is looking at heave only, these calculations can be performed manually without difficulty, see Section 3.3.

Once the mass and hydrostatic restoring matrices are checked, appropriate settings must be made in the control file. Table 3.1 shows the settings that have been modified.

Setting	**Input**
Number and range of frequencies	400 frequencies, steps of 0.02
Number of headings	10
Type of wave diffraction solution	1
Removal of irregular frequencies	No

Table 3.1: Setting in HAMS' control file.

Once HAMS has been run, the results can be visualized using the WAMIT format in BEMRosetta. A convergence study is then performed to ensure the accuracy of the results.

3.2 Geometry

This research will use a semi-submerged point absorber WEC with a cylindrical shape. The final characteristics of the WEC can be found in Table 3.2. The mesh file for the hull was modelled in Rhinoceros, see Figure 3.1.

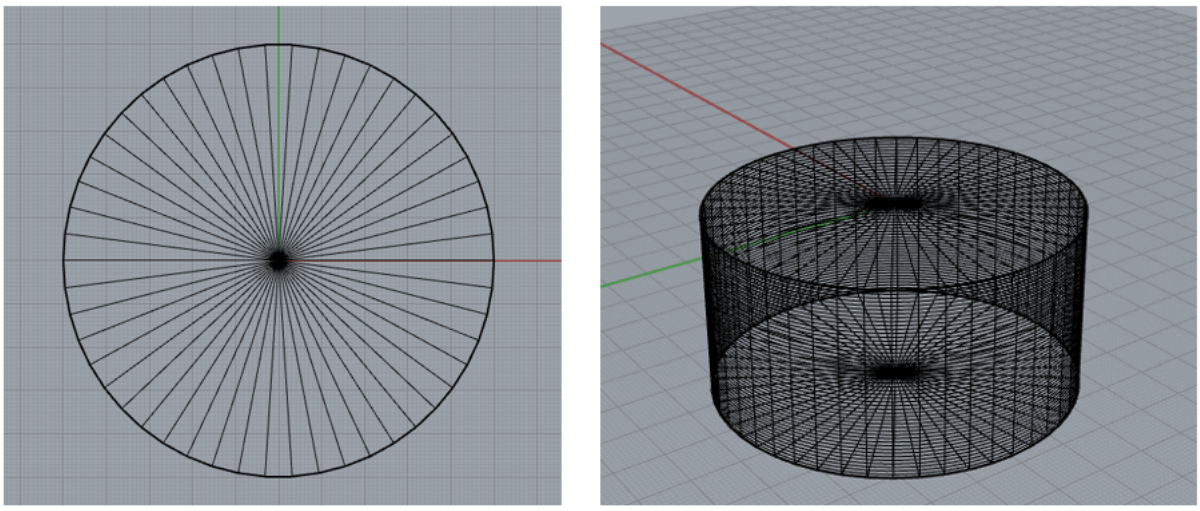

Figure 3.1: Geometry of cylindrical PA in Rhinoceros.

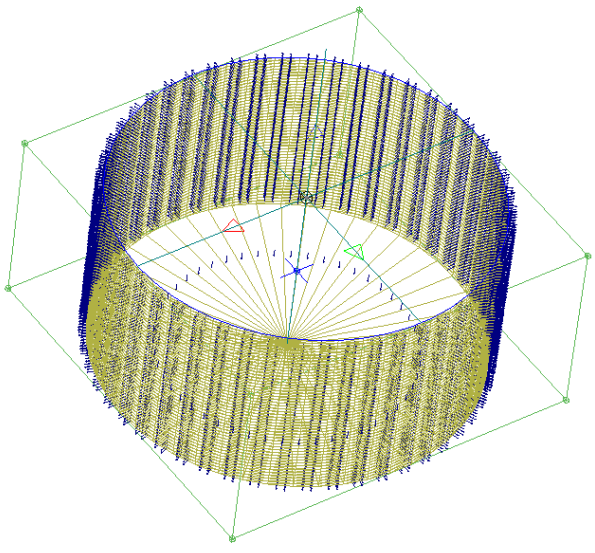

Figure 3.2: Meshfiles in BEMRosetta.

Characteristic	Value	Unit
Radius	5	m
Draft	5	m
Wetted Surface	235	m^2
Immersed Volume	392	m^3

Table 3.2: Characteristics of the WEC model.

3.3 Body Mass and Restoring Matrices

The body mass matrix is a 6x6 matrix representing the mass and inertia properties across three translational degrees of freedom (surge, sway and heave) and three rotational (roll, pitch and yaw) degrees of freedom. The first three diagonal elements therefore represent the mass [kg] in the three translational degrees of freedom respectibely, combined with added mass effects. The last three diagonal elements are related to the rotational inertia [kg.m^2] around the x-, y- and z-axis respectively. Off-diagonal terms represent coupled mass and inertia effects. This can, for example, be how a heave motion might induce pitch or roll due to the mass distribution or hydrodynamic interactions.

The hydrostatic restoring matrix represents hydrostatic forces and moments, with the first three diagonal elements indicating the surge, sway and heave hydrostatic forces in [N/m]. The last three diagonal elements represent the roll, pitch and yaw moment in [Nm/rad]. Since this research is focused on the response in heave, the hydrostatic restoring coefficiënt in heave C_{33} was manually calculated using $\rho g A$ where ρ is the fluid density, g represents the gravitational constant and A is the projected surface in heave, meaning the surface of the cylinder's base.

3.4 Convergence Study

Conducting a convergence study plays a critical role in validating a numerical model and ensuring the accuracy of simulation results. Incrementally increasing the number of panels in the hull mesh, means refining the geometrical discretization of the model. The goal of this convergence study is to show that after a certain amount of panels used in the hull mesh, the hydrodynamic coefficients stop changing while the amount of panels still increase. At this point, it can be concluded that increasing the panel count yields in negligible changes in the coefficients, which indicates that the model has reached a sufficiently detailed geometry. This level of detail is the point where the model is accurately capturing the physical responses of the system. It reassures that the numerical model is reliable and provides precise results.

The evolution of added mass, radiation damping and excitation force was investigated across multiple iterations using 220, 420, 820, 1220, 1620, 2025 and 2525 panels. The convergence study revealed that increasing the number of panels beyond 2525 resulted in negligible changes to the hydrodynamic coefficients. Given the relatively simple shape, even for a smaller number of panels, the hydrodynamic coefficients exhibited only minor variations (order of 0.01%). The hydrodynamic coefficients completely stopped changing after using 2525 panels. Consequently, all results are based on simulations performed with 2525 panels.

Vertical faces	**Around faces**	**Converter panels**
10	10	120
10	20	220
10	40	420
20	40	820
30	40	1220
40	40	1620
40	50	2025
50	50	2525
60	60	3630
100	100	10050

Table 3.3: Different iterations of numbers of panels used in the convergence study.

3.5 Mass

The properties of the cylindrical WEC in this research are comparable to those of the CorPower C4 device, as can be seen from Table 3.4. The mass for the cylindrical WEC concept in this research was therefore inspired by CorPower C4's mass, using 60,000 kg because of the height and shape difference.

	Corpower C4	**Cylindrical WEC Concept**	**Unit**
Diameter	9	10	m
Draft	6	5	m
Height	18	10	m
Installation Depth	40	41	m
Undamped Natural Period (Heave)	3	4	s
Mass	80,000	60,000	kg

Table 3.4: Propterties of CorPower C4 and the cylindrical WEC in this research [44].

3.6 Location

Two locations have been selected for a comparative analysis of wave energy resource potential. These locations were chosen based on their classification as medium and high resource areas, respectively, as indicated in the study by Lavidas and Venugopal (2017) [45].

The first location, with coordinates 58.97° N, 3.40° W, is situated in the Scottish coastal region. It is characterized by a moderate wave energy potential. Reference [45], classified this area as a medium-resource location with an available power of around 30 kW/m. The average depth for this location is 41 meters.

The second location has coordinates 58.29° N, 7.29° W and is located further offshore. Reference [45] indicates that this area consistently records higher levels of wave power, making it an ideal high-resource location with an available power of around 60 kW/m. The average depth for this location is 67 meters.

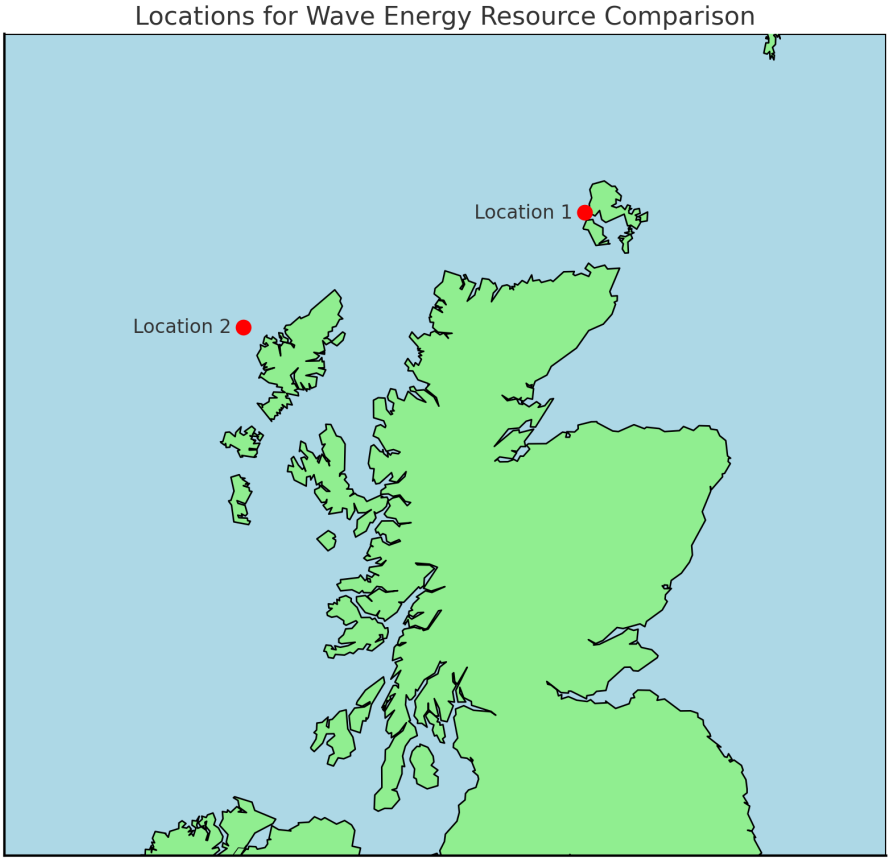

Figure 3.3: 'Two different locations considered in this research.

Results

4.1 Hydrodynamic Coefficients HAMS

Figures 4.1, 4.2 and 4.3 show the results for added mass, excitation force and radiation damping respectively. The added mass and radiation damping plots clearly indicate a spike at $\omega = 2.2\ rad/s$, possibly indicating the occurrence of an irregular frequency. No removal of irregular frequencies was performed.

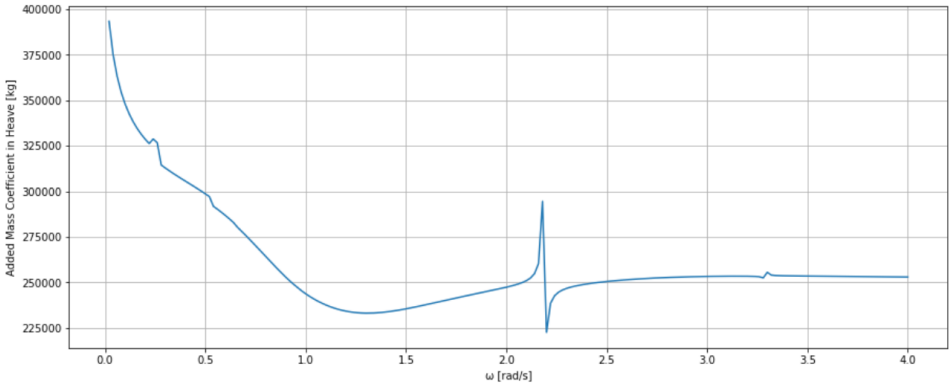

Figure 4.1: Added mass plot.

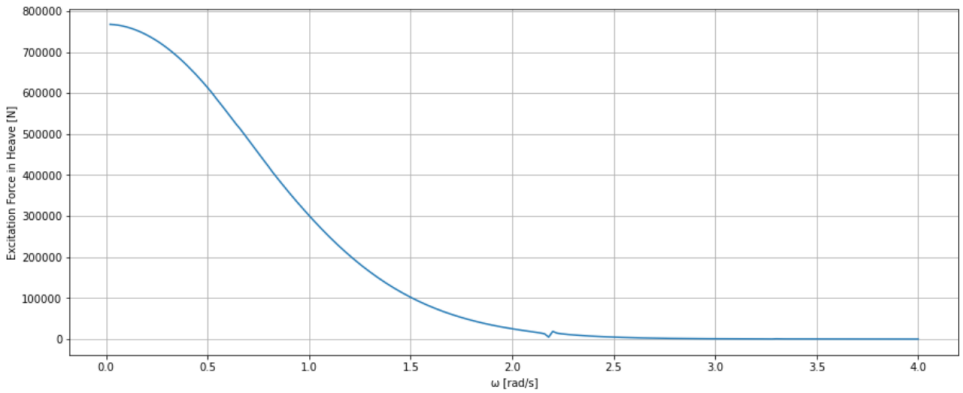

Figure 4.2: Excitation force plot.

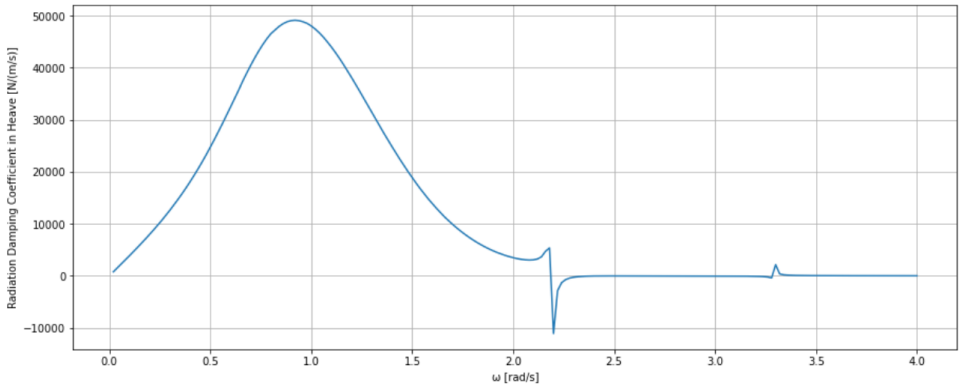

Figure 4.3: Radiation damping plot.

4.2 Undamped RAOs

Figure 4.4 shows the manually calculated response amplitude operator in heave excluding PTO damping and viscous damping, using the approach from Section 2.4. As can be seen from the figure, a peak shows at 1.62 rad/s. It is assumed that this peak is the undamped natural frequency of the cylindrical body. This was confirmed by finding the ω that sets the following expression to zero:

$$\left| \omega^2 - \frac{c}{m + m_a(\omega)} \right| \tag{4.1}$$

where $m_a(\omega)$ is the frequency-dependent added mass.Using this equation, the natural frequency was found to be 1.62 rad/s, confirming the peak in Figure 4.4.

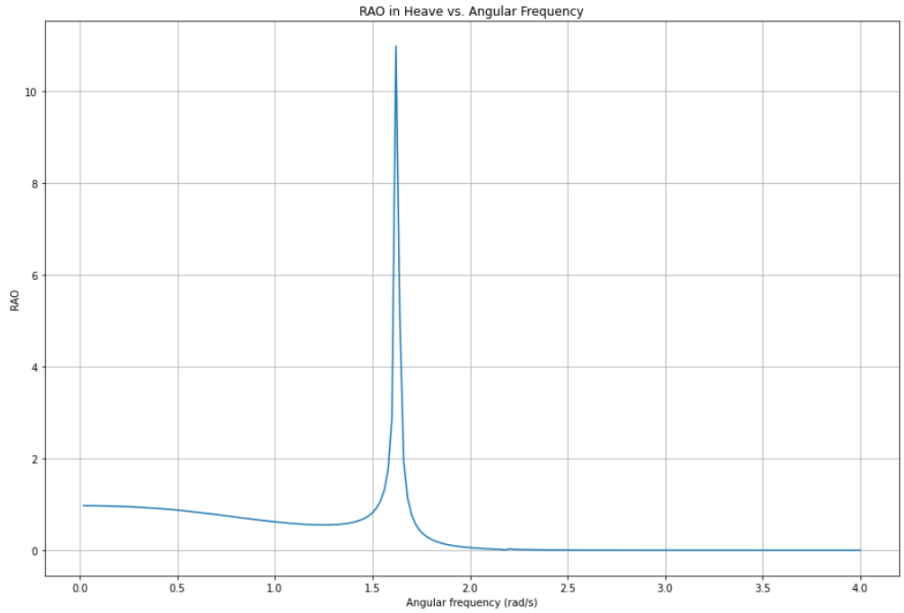

Figure 4.4: RAO in heave vs. angular frequency excluding PTO and viscous damping.

4.3 Damping Coefficients

In order to find the frequency-dependent viscous and PTO damping, the amplitudes resulting from Lorentz' Linearization need to be matched with the damped RAOs in heave, see Sections 2.3 and 2.4. This matching process was performed iteratively using a Python script. The script uses a first guess for the amplitudes and then checks whether these match the corresponding RAOs. Depending on the difference between the amplitudes and the RAOs, the amplitudes were changed and the RAOs were checked for again. This process is repeated until the correct amplitudes are found. Figure 4.5 shows how many iterations were necessary for the amplitude to match the corresponding RAO for different frequencies.

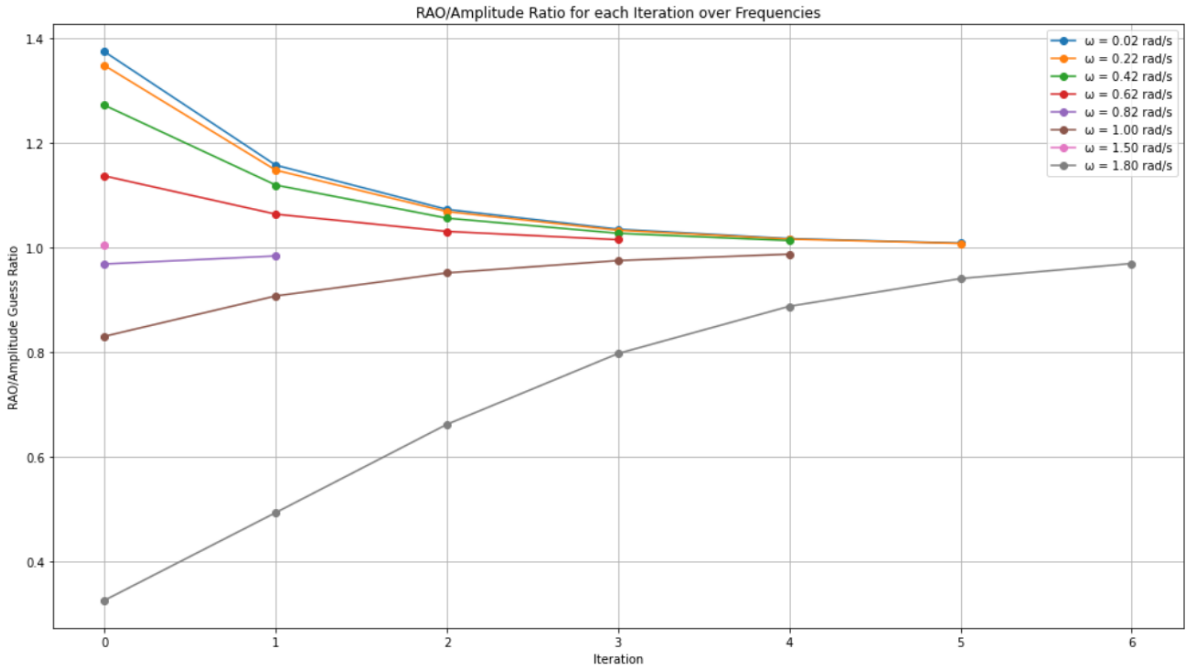

Figure 4.5: Amount of iterations necessary for amplitudes and RAOs to match, for different frequencies.

After finding the correct amplitudes, the RAOs including radiation, viscous and optimized PTO damping can be seen in Figure 4.6. The final optimized PTO damping coefficients can be seen in Figure 4.7. Note that a constant PTO damping coefficient, optimized for a single frequency, is selected to construct the power matrices, see Section 4.4.2.

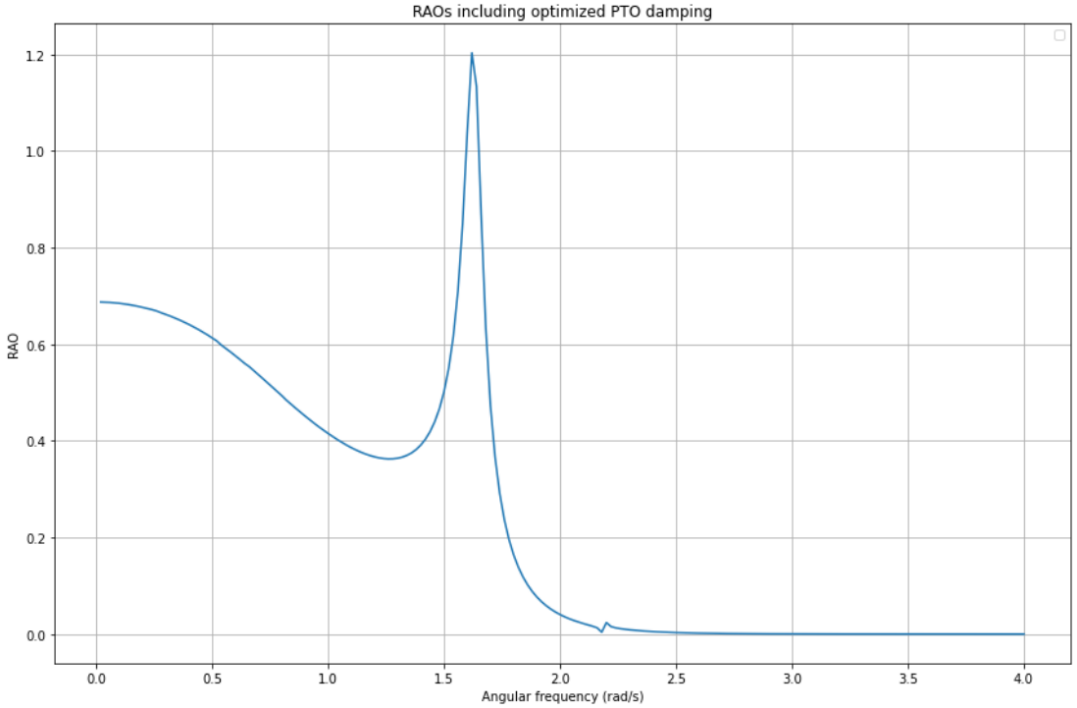

Figure 4.6: Final RAOs including radiation, viscous and optimized PTO damping.

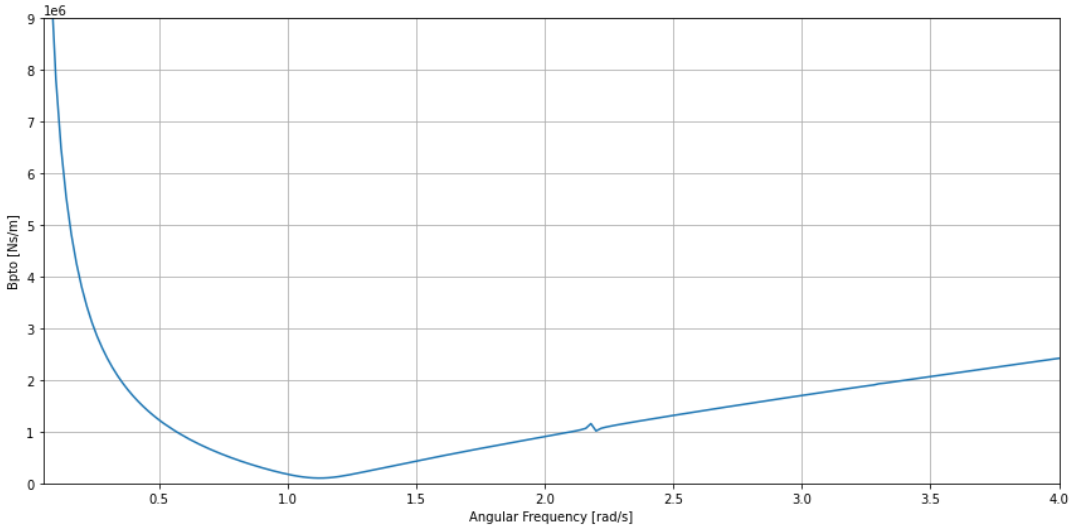

Figure 4.7: Power Take-Off damping coefficient for each frequency.

4.4 Power Estimation

In this section, the average power output of the WEC in heave is estimated for regular waves, resulting in a power matrix and estimated annual energy production. Two forms of capping will be performed. The first is power capping where a maximum power output is set for each sea state. The second method consists of putting a maximum to the PTO damping coefficient.

4.4.1 Wave Occurrence Diagram

The exact location of the wave energy converter is West of Mainland, Scotland and has coordinates North 58.97°, West -3.40°. Using the open-source ERA5 data, the ranges of the significant wave height and the peak wave period were determined. Data was used from 2008 until 2023 for every day of the month. Using this data, the wave occurrence scatter diagram in Figure 4.8 and the wave occurrence probability matrix in Figure 4.9 were constructed using Python.

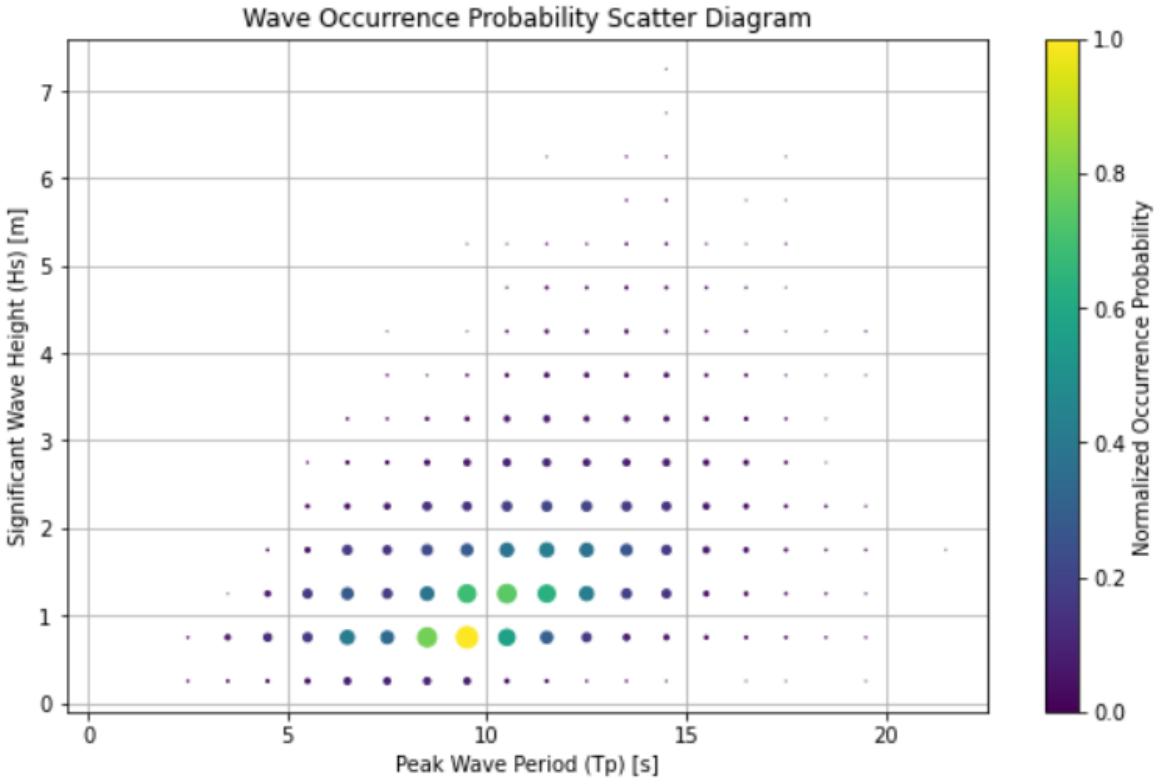

Figure 4.8: Wave occurrence scatter diagram for the chosen site.

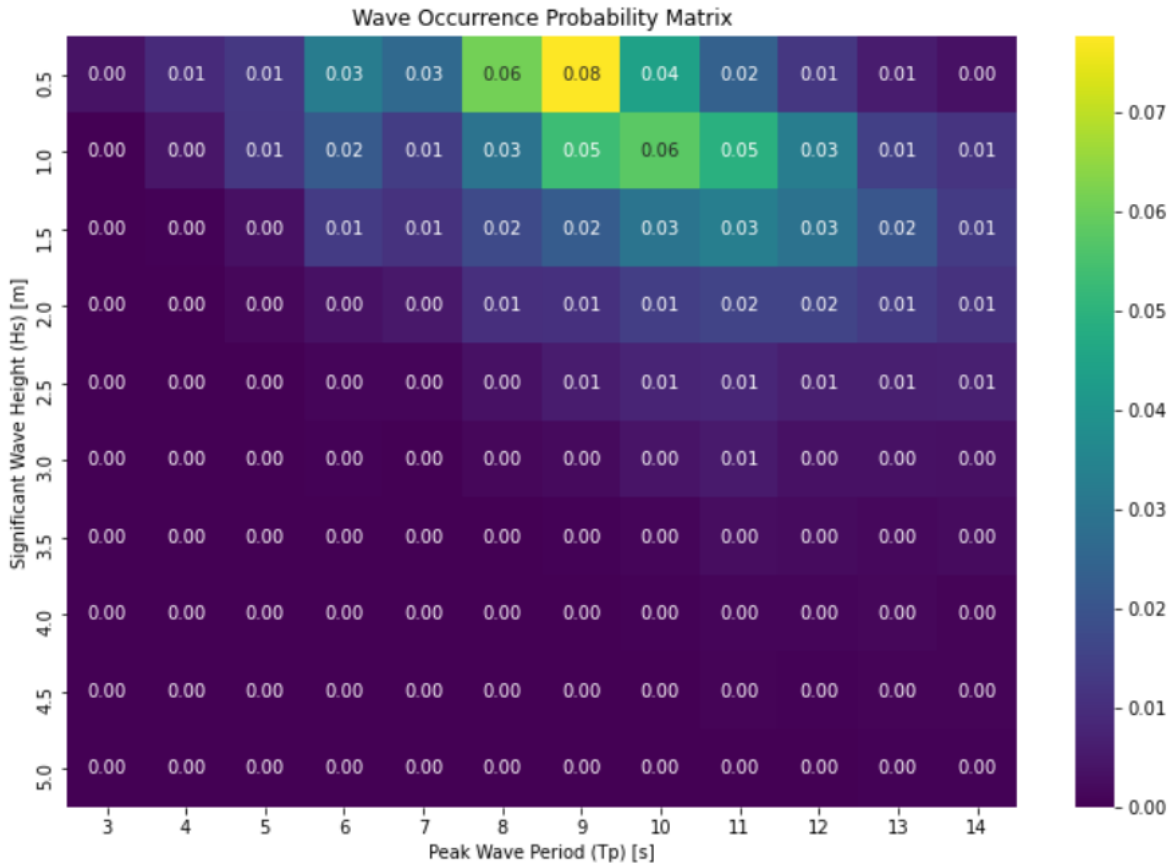

Figure 4.9: Wave occurence probability matrix.

4.4.2 Power Matrix and Annual Energy Output

Using the approach from Section 2.3, the power matrix in Figure 4.10 was constructed. Next, this power matrix, the wave occurrence probability matrix in Figure 4.9 and a generator efficiency of 70% are combined [14, 46] to estimate the AEP. For the first location, the uncapped AEP is calculated to be 235 MWh.

The presented AEP is a theoretical value assuming regular waves and a constant PTO damping coefficient. This was done to avoid outcomes that are optimized for a certain location and to avoid the PTO damping being tuned to each wave frequency. This indicates that the AEP might be overestimated and should solely be used as a value for comparison, rather than practical estimation. The constant PTO damping coefficient is equal to the optimized PTO damping coefficient at a wave period of 2.0 times the natural wave period of the undamped system to ensure a broader effective wave range [42]. The chosen coefficient also makes sure that the WEC captures energy for sea states with peak wave periods relevant to this location, with a mean wave period of roughly 8 seconds. The PTO damping coefficient was calculated to be 729 $[kNs/m]$ from the calculations presented in Section 2.3. It is important to note that the RAOs from Section 4.3 were recalculated using this constant PTO damping coefficient to construct the final power matrix.

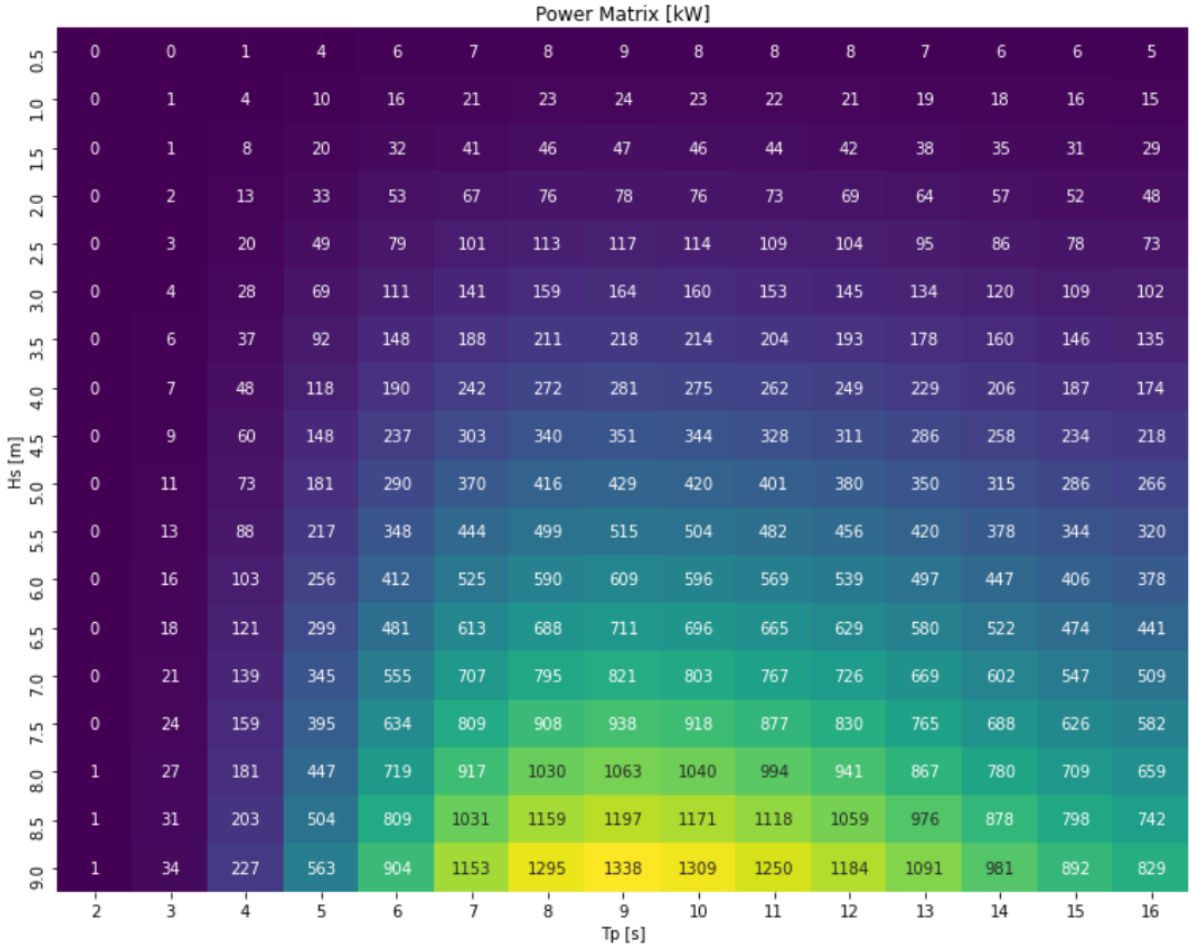

Figure 4.10: Power Matrix in kW.

4.4.3 Power Output Capping

The most direct form of power capping involves setting a maximum limit on the power output of the WEC. In order to quantify the capped amount, a scaling factor will be introduced that will quantify the maximum power output in the capped matrix, as can be seen from Equation 4.2.

$$P_{max}^{capped} = \lambda_{PC} P_{max}^{uncapped} \tag{4.2}$$

where P_{max}^{capped} is the capped maximum power output, λ_{PC} is the scaling factor for power capping and $P_{max}^{uncapped}$ is the maximum uncapped power output as calculated in the power matrix. The maximum power output is $P_{max}^{uncapped} = 1338$, corresponding to a sea state $H_s = 9.0$ m and $T_p = 9$ s. Since no PTO mechanism specifications are considered in this research, this maximum power output is considered the theoretical uncapped rated power used to calculate the capacity factor (CF), see Equation 4.3. Figures 4.11, 4.12, 4.13 and 4.14 show the four capped power matrices for scaling parameters 0.75, 0.5, 0.4 and 0.3 respectively. The relationship between λ_{PC} and CF can be seen in Figure 4.15.

$$CF = \frac{AEP}{P_{Rated} \times 8760} \tag{4.3}$$

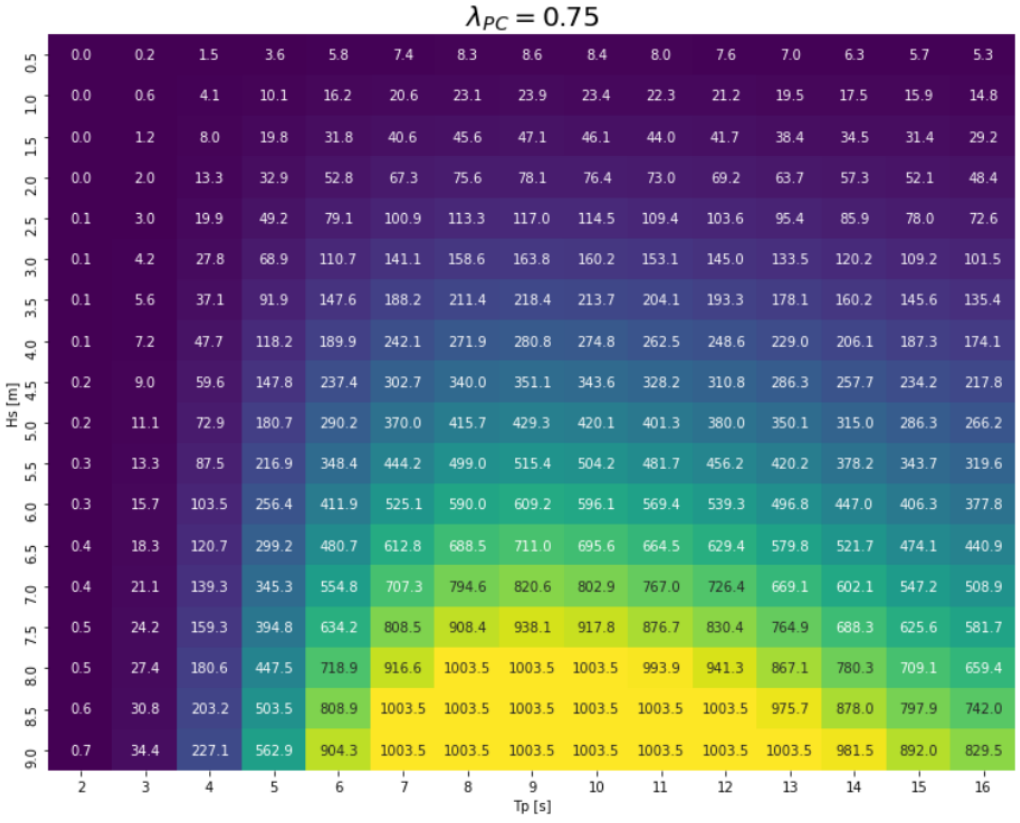

Figure 4.11: Power capped matrix with scaling factor 0.75.

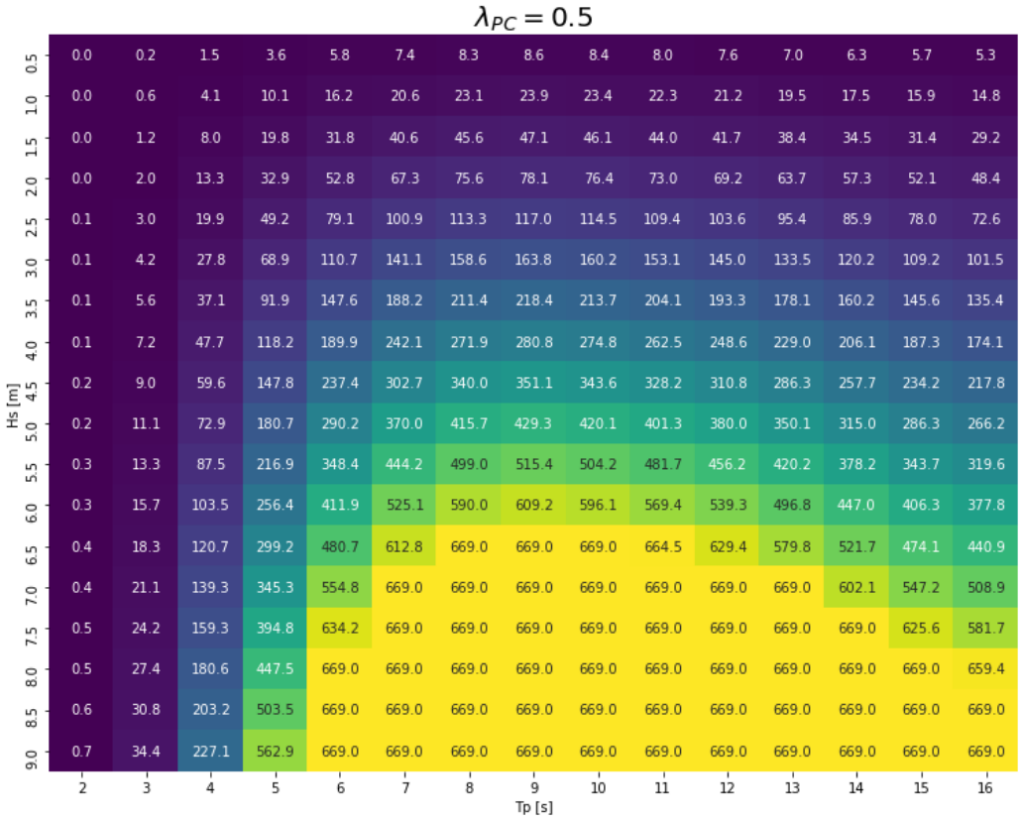

Figure 4.12: Power capped matrix with scaling factor 0.5.

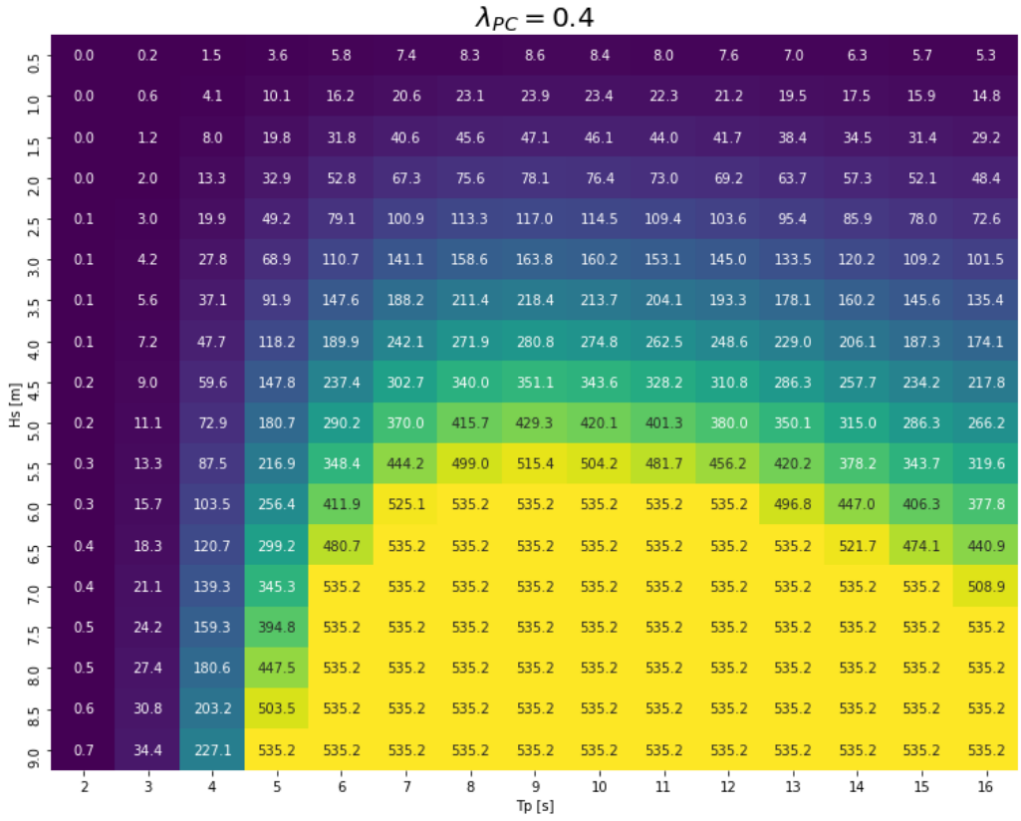

Figure 4.13: Power capped matrix with scaling factor 0.4.

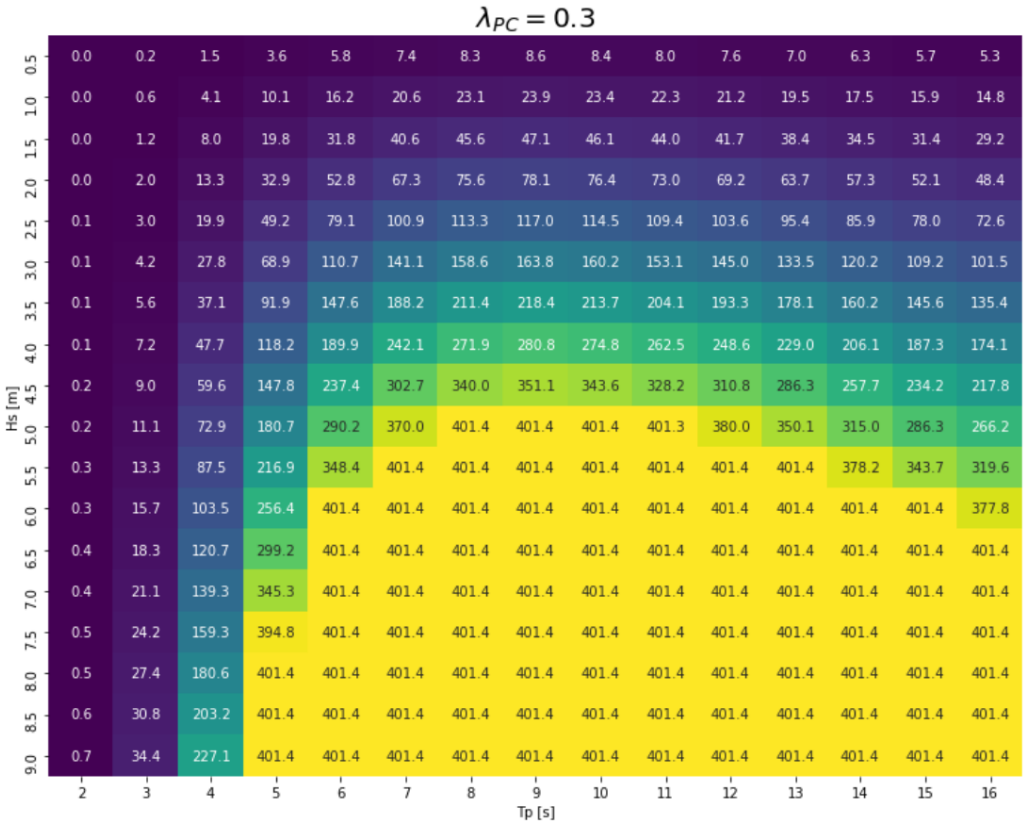

Figure 4.14: Power capped matrix with scaling factor 0.3.

Table 4.1 summarizes the influence of power capping on the AEP and the CF for each scaling factor. The theoretical rated power for the WEC in Scotland is 1338 kW, corresponding to the sea state of $H_s = 9.0$ m and $T_p = 9$ s. Scaling is performed on this uncapped rated power. Therefore, the influence of scaling on the power production is not felt for lower sea states relevant to this location. This explains why the AEP remains unchanged until very high rates of capping are performed ($\lambda_{PC} = 0.2$ or lower). What does change is the capacity factors, since the rated power changes for each scaling factor. Figure 4.15 shows the relationship between the scaling factors, the AEP (blue) and the capacity factor (red). It can be seen that the higher the rate of capping, the higher the capacity factor. This rate of increase in CF is more pronounced for higher scaling parameters, indicating an exponential relationship. This can be explained by a decrease in rated power across the scaling factors, therefore increasing the CF.

	$\lambda_{PC} = 1$	$\lambda_{PC} = 0.75$	$\lambda_{PC} = 0.5$	$\lambda_{PC} = 0.4$	$\lambda_{PC} = 0.3$	$\lambda_{PC} = 0.2$	$\lambda_{PC} = 0.1$
AEP [MWh]	235	235	235	235	235	232	219
Rated Power [kW]	1338	1004	669	535	401	268	134
CF [%]	2.00	2.67	4.01	5.01	6.68	9.94	18.68

Table 4.1: AEP, rated power and CF for each power capping scaling factor for Location 1.

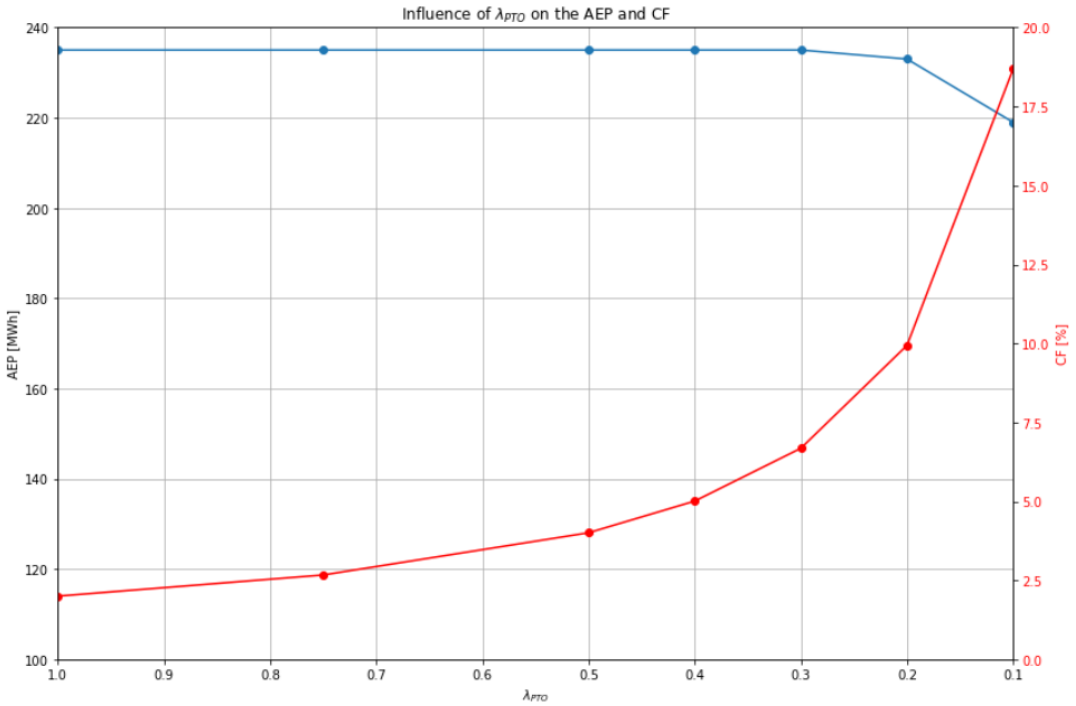

Figure 4.15: Relationship between λ_{PC}, the AEP (blue) and the CF (red) for Scotland.

4.4.4 Capping of PTO damping coefficient

A second form of power capping studied in this research is the capping of the PTO damping coefficient B_{PTO}. The same approach will be used as before, introducing a scaling factor to quantify the capped amount as shown in Equation 4.4. For each capped B_{PTO}, the RAOs are recalculated and the power matrices are constructed following the method as described in Section 2.3.

$$B_{PTO}^{capped} = \lambda_{PTO} B_{PTO}^{uncapped} \tag{4.4}$$

where B_{PTO}^{capped} is the capped maximum PTO damping coefficient, λ_{PTO} is the scaling factor for PTO capping and $B_{PTO}^{uncapped}$ is the uncapped constant PTO damping coefficient B_{PTO} equal to 729 [kNs/m]. Figures 4.16, 4.17, 4.18 and 4.19 show four capped power matrices for scaling parameters 0.75, 0.5, 0.4 and 0.3 respectively. The corresponding AEP for the location in Scotland can be found in Table 4.2. The relationship between λ_{PTO}, the AEP and the CF is visualized in Figure 4.20.

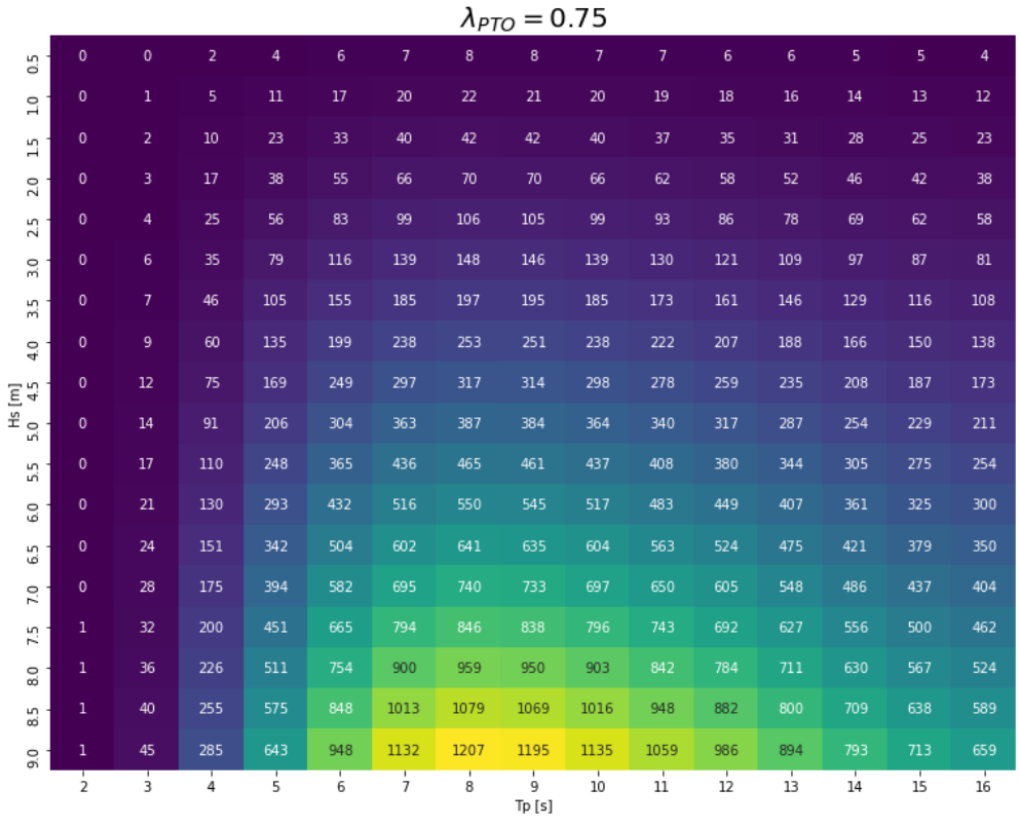

Figure 4.16: PTO capped matrix for scaling factor 0.75

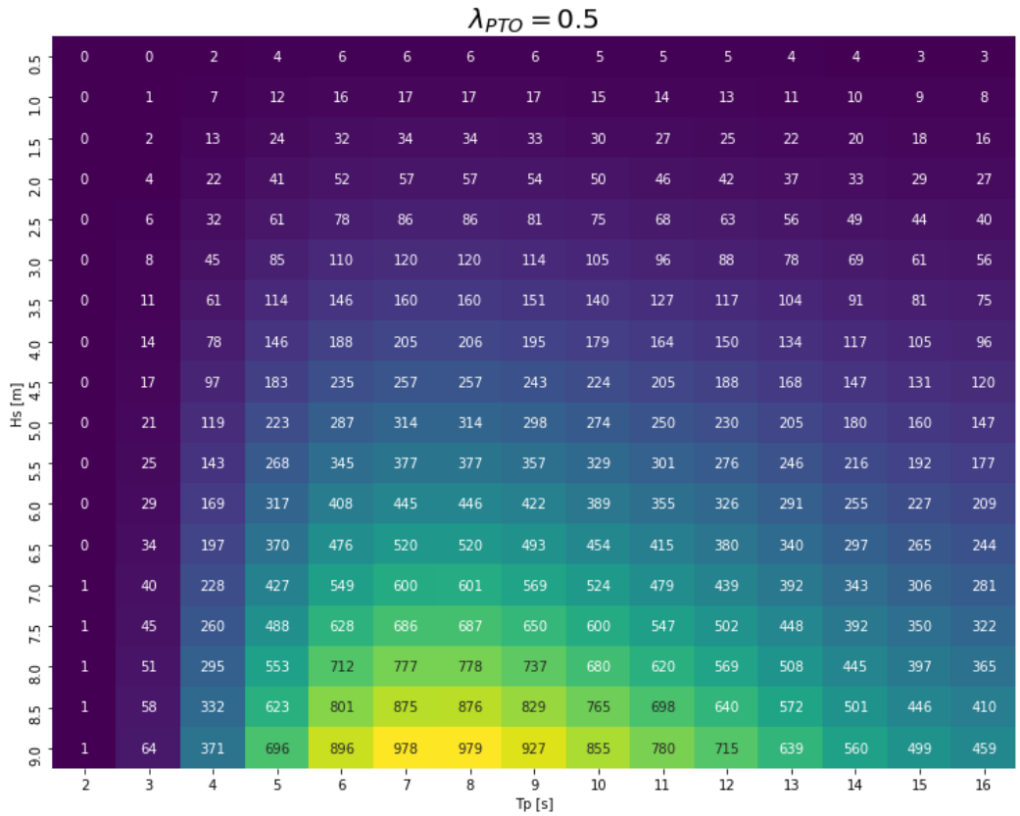

Figure 4.17: PTO capped matrix for scaling factor 0.5.

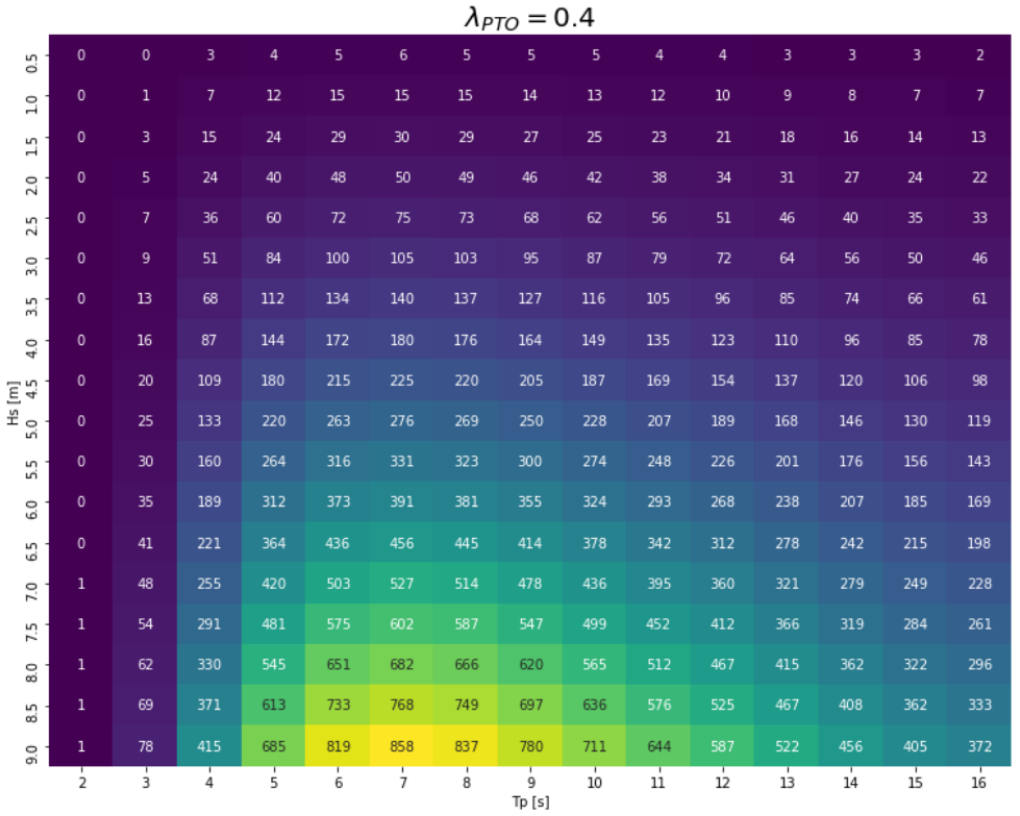

Figure 4.18: PTO capped matrix for scaling factor 0.4.

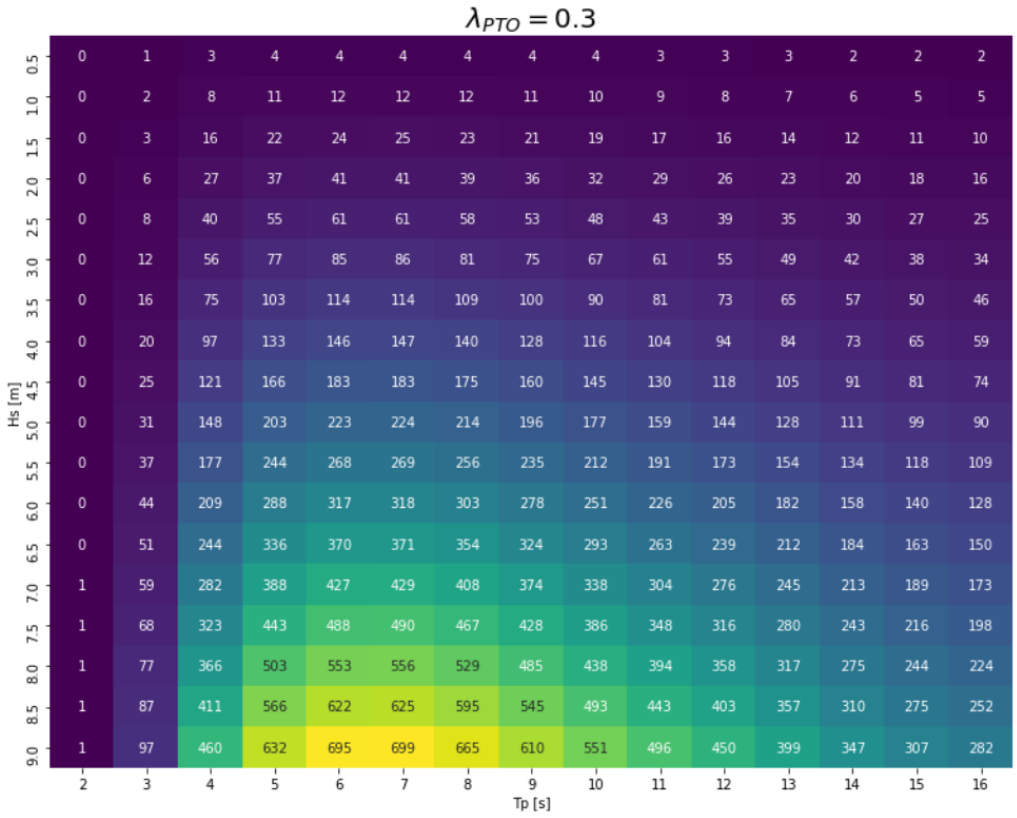

Figure 4.19: PTO capped matrix for scaling factor 0.3.

Table 4.2 summarizes the influence of PTO damping capping on the AEP and the CF for each scaling factor. In contrast to power capping, PTO damping capping influences all sea states. This results in a decrease in AEP across all scaling factors. Since both the rated power and the AEP are decreasing at similar rates, the capacity factor remains relatively constant across the scaling factors.

Figure 4.20 shows an approximately linear relationship between PTO damping capping and the AEP across the scaling factors. This can be explained by the absorbed power formula from Section 2.5. The absorbed power is directly related to the PTO damping coefficient, as well as to the corresponding RAOs. It is also important to note that by increasing the cap on the PTO damping, the rated power corresponds to sea states with lower wave periods as can be seen from Figures 4.16 to 4.19.

	$\lambda_{PTO} = 1$	$\lambda_{PTO} = 0.75$	$\lambda_{PTO} = 0.5$	$\lambda_{PTO} = 0.4$	$\lambda_{PTO} = 0.3$	$\lambda_{PTO} = 0.2$	$\lambda_{PTO} = 0.1$
AEP [MWh]	235	203	155	130	101	70	36
Rated Powers [kW]	1338	1207	979	858	699	516	429
CF [%]	2.01	1.92	1.81	1.73	, 1.65	1.55	0.96

Table 4.2: AEP, rated power and CF for each PTO damping scaling factor for Location 1.

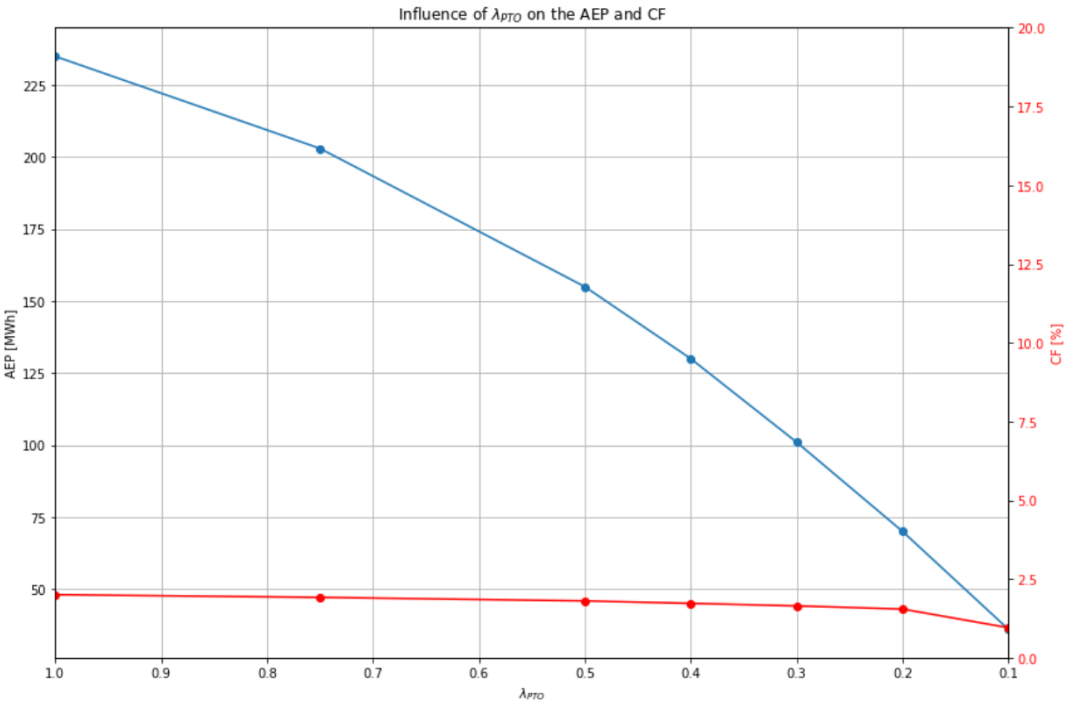

Figure 4.20: Relationship between λ_{PTO} the AEP (blue), and the CF (red) for Scotland.

4.5 High energy region

Using the open-source ERA5 data, the wave occurrence scatter diagram in Figure 4.21 and the wave occurrence probability matrix in Figure 4.22 were constructed. As can be seen from these figures, the second location covers sea states with higher significant wave heights in comparison to the first location.

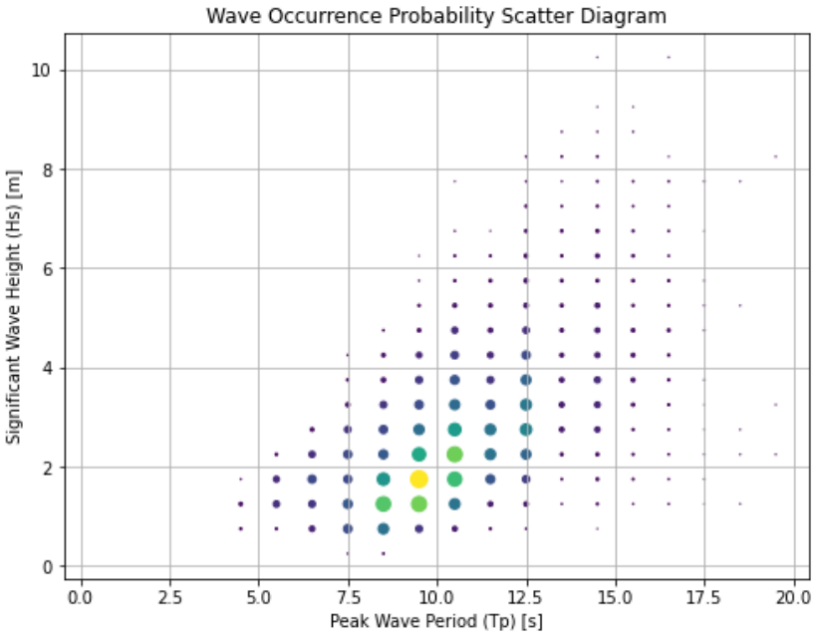

Figure 4.21: Wave scatter diagram for location 2.

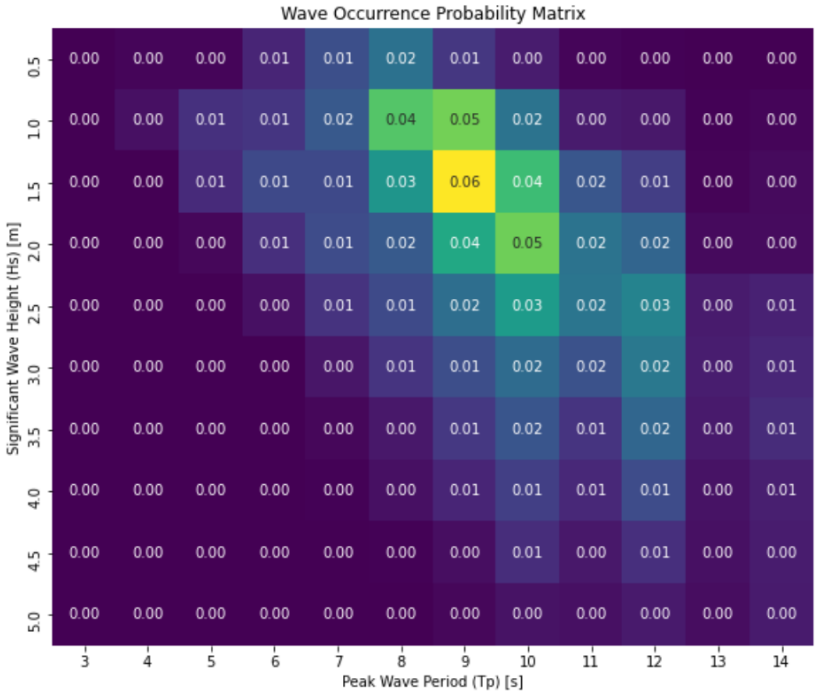

Figure 4.22: Wave occurrence probability matrix for location 2.

The same approach was used as before. The hydrodynamic coefficients were calculated using HAMS, this time considering a depth of 67 meters instead of 41 meters. Changes in these coefficients were expected and confirmed to be minimal. Again, a power matrix was constructed using regular waves. The result can be found in Figure 4.23. Both power and PTO capping were performed. The relationship between the scaling factor and the AEP for this high-energy region can be found in Tables 4.3 and 4.4 for power and PTO capping respectively.

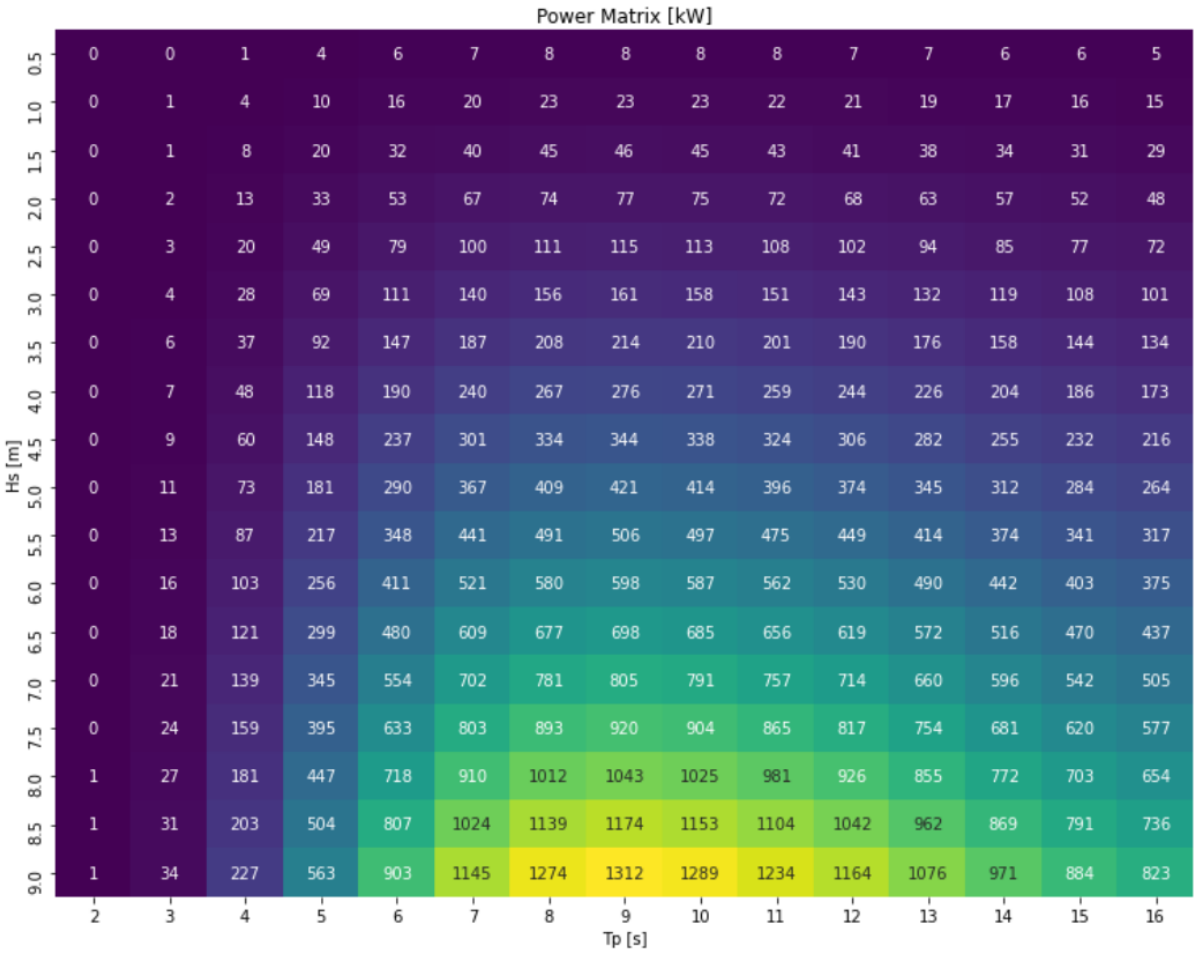

Figure 4.23: Power Matrix for Location 2.

As can be seen from Figure 4.24, the relationship between λ_{PC} and the AEP is comparable to the medium-energy region. The difference is that the drop in AEP starts earlier from lower amounts of capping. The reason for this is that more sea states with higher significant wave heights occur in the high-energy location. As λ_{PC} decreases, the AEP decreases as well. The rate of this decrease becomes more pronounced for higher capping rates. From Figure 4.24, it can be seen that the scaling factor and CF have an exponential relationship, which was the same case for the medium-energy region. The only difference is that this exponential relationship is more pronounced for the medium-energy region, where the CF increased by 834%, whereas for the high-energy region, the CF increased by 594% under the strictest power cap.

	$\lambda_{PC} = 1$	$\lambda_{PC} = 0.75$	$\lambda_{PC} = 0.5$	$\lambda_{PC} = 0.4$	$\lambda_{PC} = 0.3$	$\lambda_{PC} = 0.2$	$\lambda_{PC} = 0.1$
AEP [MWh]	683	683	680	674	657	612	474
Rated Power [kW]	1312	984	656	525	394	262	131
CF [%]	5.94	7.92	11.83	14.66	19.05	26.62	41.24

Table 4.3: AEP, rated power and CF for each power capping scaling factor for location 2.

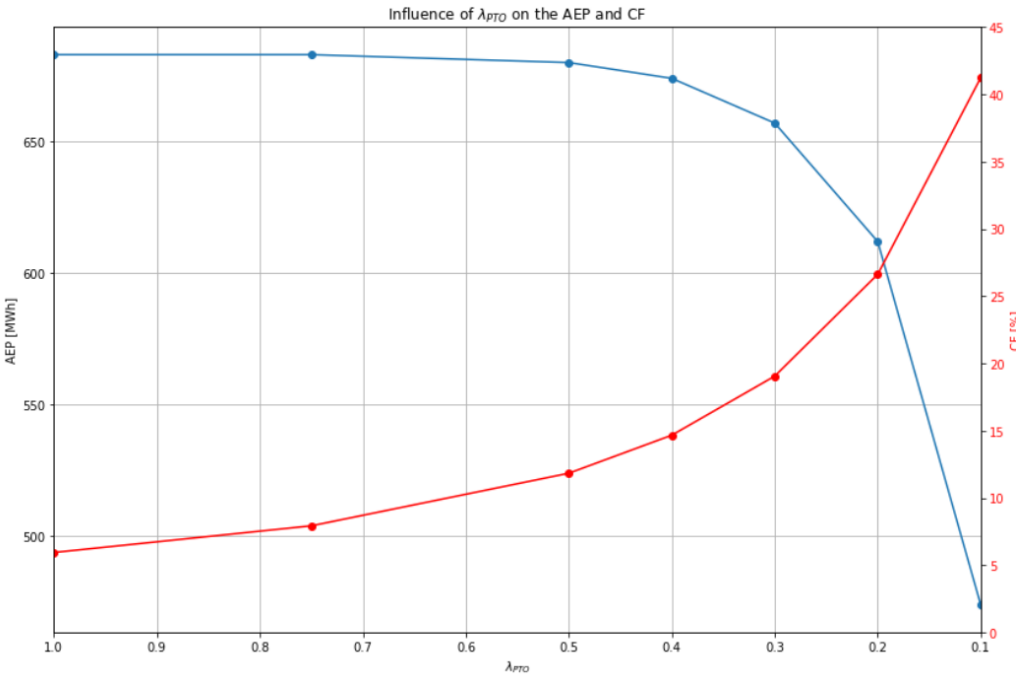

Figure 4.24: Relationship between λ_{PC}, the AEP (blue) and the CF (red) for Location 2.

As can be seen from Figure 4.25, the relationship between λ_{PTO} and AEP is approximately linear, which was the same for the medium-energy region. The AEP drops significantly from 683 MWh to 100 MWh under the strictest cap. Again, the capacity factor stays relatively constant across the scaling factors. As said before, this can be confirmed by the equal rates of changes in AEP and rated powers, therefore keeping the CF almost constant.

	$\lambda_{PTO} = 1$	$\lambda_{PTO} = 0.75$	$\lambda_{PTO} = 0.5$	$\lambda_{PTO} = 0.4$	$\lambda_{PTO} = 0.3$	$\lambda_{PTO} = 0.2$	$\lambda_{PTO} = 0.1$
AEP [MWh]	683	588	442	368	286	196	100
Rated Powers [kW]	1312	1187	971	852	694	515	428
CF [%]	5.94	5.65	5.20	4.93	4.70	4.34	2.67

Table 4.4: AEP, rated power and CF for each PTO damping scaling factor for Location 2.

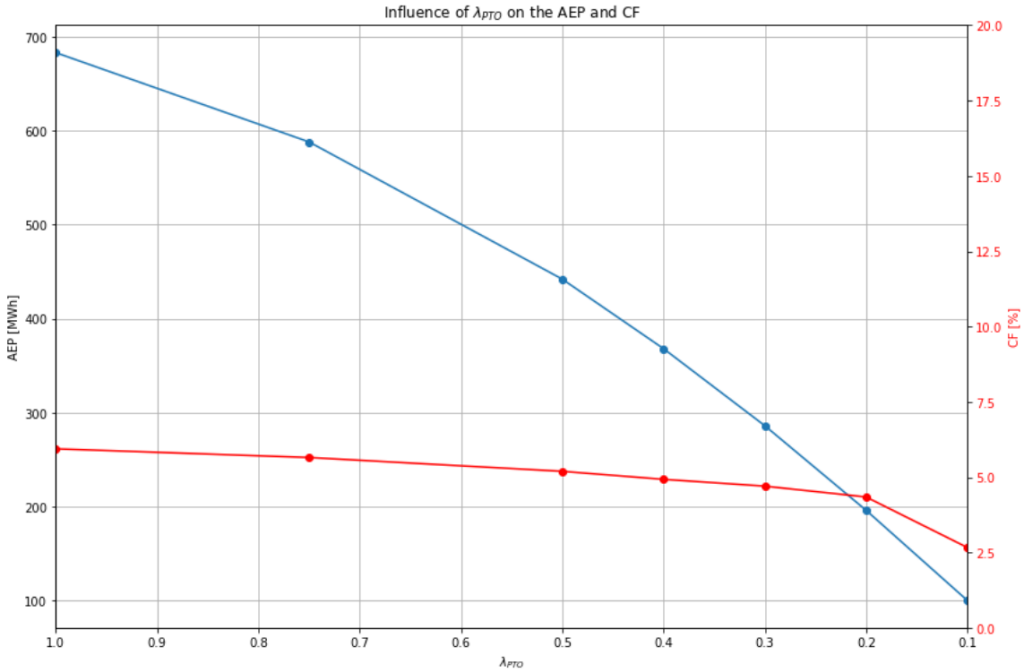

Figure 4.25: Relationship between λ_{PTO}, the AEP (blue) and the CF (red) for Location 2.

4.5.1 Comparison Between Medium- and High-Energy Regions

The analysis of power capping and PTO damping capping shows a big impact on the AEP for both medium and high energy regions. The influence of power capping in the medium-energy region resulted in a decrease in AEP of 7% under the strictest cap (λ_{PC} = 0.1), whereas in the high-energy region, this decrease in AEP was 31%.

The difference can be explained by the wave scatter diagrams. In high-energy regions, there are more frequent sea states with higher significant wave heights, which contribute significantly to the power output. When power capping is applied, these high-energy sea states are affected even at lower capping rates, leading to a larger reduction in AEP. On the other hand, in medium-energy regions, the occuring sea states have lower significant wave heights and thus lower power outputs. Therefore, more severe capping (lower λ_{PC}) is required to significantly impact the AEP for these medium-energy sea states.

The influence of power capping on the capacity factors is similar for medium- and high-energy regions, both showing an exponential relationship between the CF and the scaling factors. The increase in CF for the medium-energy region is more significant across the scaling factors used (834% increase), in comparison to the high-energy region (594% increase). This can be explained by the difference in the decrease of AEP for both regions. In the medium-energy region, there was a relatively small decrease in AEP. Therefore, the CF was almost solely dependent on the increase in rated power. Whereas for the high-energy region, the decrease in AEP for higher capping rates slowed down the increase in CF.

The influence of PTO damping capping was identical for both regions, showing an almost linear relationship between the AEP and the scaling factors. For both locations, the decrease in AEP was found to be 85%. Due to the equal rates in decrease of the AEP and the rated power, the CF stays almost constant across all scaling factors for both the medium- and high-energy regions. The only differences are the absolute values of AEP and CF, due to the higher resource availability in the high-energy region.

Economical Assessment

5.1 Economical Model

In this chapter, an economical assessment is performed, computing the capital (CAPEX) and operational expenditure (OPEX) of this research's WEC. Based on the CAPEX and OPEX, the LCOE can be obtained. The LCOE is a widely used concept throughout the energy generation industry to assess a project's profitability.

LCOE is defined as the total capital, operational and maintenance costs associated with the generation, discounted to the present-day value, divided by the electricity delivered to the grid throughout the project's operational life. The following equation shows the LCOE calculation, where LCOE is the levelized cost of electricity, CAPEX is the capital expenditures, OPEX is the operational expenditures, AEP is the annual energy production, n is the lifespan of the project and r is the discount rate.

$$\text{LCOE} = \frac{\text{CAPEX} + \sum_{t=1}^{n} \frac{\text{OPEX}_t}{(1+r)^t}}{\sum_{t=1}^{n} \frac{\text{AEP}_t}{(1+r)^t}} \tag{5.1}$$

5.1.1 CAPEX

In order to derive the CAPEX, the methodology Tan et al. (2021) is adopted [14]. The different cost components of the CAPEX considered in this economical model can be found in Equation 5.2.

$$CAPEX = C_{mass} + C_{power} \tag{5.2}$$

where

$$C_{mass} = C_{structure} + C_{foundation} + C_{installation} \tag{5.3}$$

$$C_{power} = C_{PTO} + C_{connection} \tag{5.4}$$

Since the objective of this research is to see the influence of power capping on the LCOE, rather than looking at the integration to the grid, the cost of connection $C_{connection}$ is considered to be 0.

Following Tan et al. (2021), the different components of the CAPEX can be expressed as percentages of the total CAPEX [14]. The percentages of these components

related to the LCOE were used from the study by De Andres et al. (2017) [46] and then recalculated as the average percentage in total CAPEX. Using these calculations, the mass-related capital cost can be expressed as in Equation 5.5. The percentages of the CAPEX components relative to the total CAPEX can be found in Table 5.1. It must be noted that these percentages are based on averages. Since this research's aim is to compute a theoretical LCOE rather than an optimized one, this approach is assumed reasonable.

$$C_{mass} = (\frac{P_F}{P_S} + \frac{P_I}{P_S} + 1)C_{structure} \tag{5.5}$$

Classification	Symbol	Average Percentage
Structure	P_S	38.2%
Foundation	P_F	19.1%
Installation	P_I	10.2%

Table 5.1: Percentages of CAPEX components relative to total CAPEX [14].

The cost of the power take-off mechanism is mainly dependent on the linear generator [14, 47]. It is beyond the scope of this research to delve into the specifications of different types of linear generators. Therefore, the price of the linear generator is based on its assumed weight and compared to the linear generator used by reference [48]. In the paper, a point-absorber device developed by Uppsala University Sweden is economically assessed [49]. It was considered that the total mass mainly consisted of the mass of the buoy (30.77%) and the mass of the generator (69.23%). These percentages are applied to the total mass of 60,000 kg in this research, to provide an estimate for the buoy and generator masses.

In order to account for the manufacturing cost of the generator, 50% of the material costs is taken into account [50]. Since the costs in reference [48, 14] are both for the year 2020, inflation needs to be taken into account. Inflation in Europe has reached historical peaks during the period from 2021 until 2024. The used inflation rates are 0.25%, 2.60%, 8.38% and 5.48% for 2020, 2021, 2022 and 2023 respectively [51, 52, 53]. The resulting prices used for the CAPEX calculation can be found in Table 5.3 [48]. The price for the generator is estimated based on casing, translator and stator materials. Foundation is included as a percentage, as can be seen from Table 5.1. The cost of the stator is based on the cost of the copper windings and the cost of the buoy is calculated based on the cost of the steel, all taking into account the inflation rates as presented. The labour costs are estimated for one month of work for five people. The material costs considered can be found in Table 5.2.

Material	Value	Unit
Steel	2.47	EUR/kg
Copper	3.53	EUR/m
Concrete	147	EUR/m^3

Table 5.2: Material costs taking into account inflation since 2020 [14].

Description	Symbol	Value	Unit
Buoy	$C_{structure}$	2.47	EUR/kg
Generator	C_G	4.51	EUR/kg
Generator Manufacturing	C_{PTO}	2.25	EUR/kg

Table 5.3: Cost estimations for one WEC taking into account inflation since 2020.

5.1.2 OPEX

The OPEX accounts for the costs relating to the maintenance and repair of the buoy and the generator throughout its lifetime. It should be noted that this is an initial economic model and the parameters within the model can vary from one project to another in real-world applications. As a result, power control strategies, such as power capping, can influence the OPEX [14]. However, these specific impacts are tied to the PTO design and its maintenance, which is beyond the scope of this research. Considering the objective to determine the impact of power capping on techno-economic performance, it is considered reasonable to assume a constant OPEX percentage for both the uncapped and capped scenarios. The annual OPEX is assumed to be 8% of the CAPEX [54, 46, 55]. A discount rate of 8% and a project lifespan of 20 years were chosen [54, 46].

5.2 Economical Results

5.2.1 Medium-Energy Region

The results of the calculations can be found in Table 5.4 and 5.5 for the capped power and capped PTO damping coefficient respectively.

	Uncapped	**Capped Power**				Unit
		$\lambda_{PC} = 0.5$	$\lambda_{PC} = 0.4$	$\lambda_{PC} = 0.3$	$\lambda_{PC} = 0.2$	
CAPEX	361,376	361,376				EUR
OPEX	28,910	28,910				EUR
Theoretical AEP	235	235	235	235	232	MWh
LCOE	280	280	280	280	283	EUR/MWh

Table 5.4: Comparison of financial metrics for uncapped vs. capped power settings for Location 1.

	Uncapped	**Capped PTO Damping Coefficient**				Unit
		$\lambda_{PTO} = 0.5$	$\lambda_{PTO} = 0.4$	$\lambda_{PTO} = 0.3$	$\lambda_{PTO} = 0.2$	
CAPEX	361,376	361,376				EUR
OPEX	28,910	28,910				EUR
Theoretical AEP	235	155	130	101	70	MWh
LCOE	280	424	506	651	939	EUR/MWh

Table 5.5: Comparison of financial metrics for uncapped vs. capped PTO damping coefficient settings for Location 1.

As can be seen from Table 4.1, the change from uncapped to capping with a high scaling factor ($\lambda_{PC} = 0.2$) only results in a minimal increase in LCOE from 280 EUR/MWh to 283 EUR/MWh. This result is directly related to the AEP across the scaling factors, which stays almost constant for the medium-energy region. The influence of power capping in the medium-energy region on the LCOE can therefore be concluded to be minimal. This is due to the relatively high rated power in comparison to the power production for the lower sea states relevant to this location.

Capping the PTO damping coefficient has a big impact on the LCOE of the WEC. The economic implications are large, with LCOE rising to 939 EUR/MWh in the most restrictive damping scenario. This increase indicates a big impact on the cost-effectiveness of the system. An increase in LCOE of 235% is observed from uncapped to the strictest PTO damping cap scenario ($\lambda_{PTO} = 0.2$). From the two tables, it can be concluded that capping of the PTO damping coefficient tends to reduce the energy capture efficiency more significantly than straightforward power capping, resulting in a much sharper increase in LCOE.

5.2.2 High-Energy Region

	Uncapped	**Capped Power**				Unit
		$\lambda_{PC} = 0.5$	$\lambda_{PC} = 0.4$	$\lambda_{PC} = 0.3$	$\lambda_{PC} = 0.2$	
CAPEX	361,376	361,376				EUR
OPEX	28,910	28,910				EUR
Theoretical AEP	683	680	674	657	612	MWh
LCOE	96	97	98	100	107	EUR/MWh

Table 5.6: Comparison of financial metrics for uncapped vs. capped power settings for Location 2.

	Uncapped	**Capped PTO Damping Coefficient**				Unit
		$\lambda_{PTO} = 0.5$	$\lambda_{PTO} = 0.4$	$\lambda_{PTO} = 0.3$	$\lambda_{PTO} = 0.2$	
CAPEX	361,376	361,376				EUR
OPEX	28,910	28,910				EUR
Theoretical AEP	683	442	368	286	196	MWh
LCOE	96	149	179	230	335	EUR/MWh

Table 5.7: Comparison of financial metrics for uncapped vs. capped PTO damping coefficient settings for Location 2.

As can be seen from Tables 5.6 and 5.7, there is a big difference in LCOE between power capping and PTO damping capping. For power capping, the change from uncapped to capping with a high scaling factor ($\lambda_{PC} = 0.2$) only slightly decreases the AEP. This reduction in AEP is accompanied by an increase in the LCOE, which changes from 96 EUR/MWh in the uncapped scenario to only 107 EUR/MWh under the strictest cap, corresponding to an increase of 11%. This minimal change in AEP and LCOE is slightly bigger compared to the results from the medium-energy region, where the increase in LCOE was only 1%.

Similarly to the medium-energy region, capping the PTO damping coefficient has a significant effect, which is more pronounced than simple power capping. The LCOE rises to 335 EUR/MWh in the most restrictive damping scenario. This corresponds to an increase in LCOE of 249% from uncapped to the strictest PTO damping cap scenario. From the two tables, it can be seen that capping the PTO damping coefficient tends to reduce the energy capture efficiency more significantly than straightforward power capping, resulting in a sharper increase in LCOE. This trend is consistent with the observations from the medium-energy region. The absolute values of the medium-energy region's LCOE are higher due to a lower AEP.

5.2.3 Comparison Between Medium- and High-Energy Region

When comparing medium- and high-energy regions, despite identical CAPEX and OPEX, significant differences are observed in the percentage changes of LCOE due to variations in the AEP. In the medium-energy region, characterized by lower uncapped AEP, the impact of power capping on the LCOE was found to be minimal, with an increase in LCOE of only 1% under the strictest capping scenario. This was different from the high-energy region, where power capping led to an increase of 11% in LCOE. As stated before, this is due to the difference in wave scatter diagrams. Sea states with higher significant wave heights contribute more substantially to the power output. When power capping is performed, these sea states are affected, even at lower capping rates. This leads to a larger reduction in AEP and, consequently, to a larger increase in LCOE.

When looking at PTO damping capping, both regions showed similar results, with increases in LCOE of 235% and 249% for the medium- and high-energy regions respectively. As stated in Section 4.5.1, the AEP shows an almost linear relationship with the scaling factors. This results in a linear increase in LCOE across the scaling factors for both regions.

The comparison between both locations shows that WECs in high-energy regions, while benefiting from higher initial AEPs, also exhibit greater economic losses in response to power capping. This sensitivity can be seen in steeper increases in LCOE for power capping, resulting from larger proportional reductions in AEP in comparison to the medium-energy region. For PTO damping capping, the increase in LCOE was similar for both regions, but still slightly higher for the high-energy region. When comparing power capping and PTO damping capping, the increase in LCOE is way more significant for PTO damping capping, with costs escalating 2136% higher relative to power capping in the high energy region, calculated from an 11% increase versus a 249% increase for the different capping methods.

Conclusions

This thesis investigated the influence of limiting power production on the LCOE in wave energy, specifically examining the effects through numerical modelling and a comparative analysis between capped and uncapped scenarios across two different wave resource energy regions. Using a cylindrical point absorber in heave, the study used HAMS software to derive hydrodynamic coefficients and construct power matrices under regular wave conditions to maintain objectivity and avoid location-specific optimizations.

Using the results obtained throughout this thesis, the research questions as presented in Section 1.2 will be answered. The primary objective of this research is to assess the following:

'What is the influence of limiting power production on the levelized cost of electricity in wave energy?'

The sub-research questions proposed to fully answer the main research question are:

- *'How can numerical modelling be used to compute the theoretical annual energy production of WECs? What open-source software is most useful in this case?'*
- *'How can the power take-off damping coefficient be calculated?'*
- *'How can a power matrix be constructed from numerically calculated hydrodynamic parameters?'*
- *'How does capping influence the annual energy production of WECs and therefore the LCOE? Is there a large difference between power output capping and power take-off capping?'*
- *'Does capping have a similar influence on the LCOE in medium and high energy regions?'*

A comparative analysis between three BEM solvers HAMS, WAMIT and NEMOH was performed. A final comparison showed that HAMS was a balanced option between NEMOH's relatively long computation time and WAMIT's commercial nature. The possibility of further exploring HAMS' potential due to its more recent introduction, is what pushed the final choice between the three options.

The damping force was linearized using Lorentz' Linearization, an alternative to the more familiar Fourier transform. Using this linearization, a frequency-dependent power

take-off damping coefficient was constructed, taking into account viscous losses. A constant PTO damping coefficient was finally used, based on the natural period of the WEC, keeping in mind the objective to obtain a general outcome rather than an optimized one. A power matrix was constructed considering regular wave conditions, again to avoid optimization for a certain location. The RAOs used for the power matrix were calculated by hand.

The use of scaling factors was introduced to quantify the amount of capping performed on the power output. Both power capping and PTO damping capping were implemented. Power capping involves limiting the maximum energy produced, while PTO damping capping involves limiting the PTO damping coefficient, requiring RAOs to be recalculated accordingly. The comparison between power output capping and PTO damping capping showed that both methods lead to an increased LCOE, but the rate and impact of the increase varied. It was found that PTO capping results in a sharper increase in LCOE in comparison to power capping, with costs escalating 234% higher relative to power capping under the strictest scenario.

This conclusion was further substantiated by a comparison in a high-energy region. Introducing a second location confirmed that capping leads to a reduction in AEP, which in turn increases the LCOE. However, for power capping, the extent of this effect was more pronounced in the high-energy region. In the medium-energy region, an increase in LCOE of only 1% was seen for power capping. For the high-energy region, this increase was calculated to be 11%. In both regions, PTO damping capping has a significantly more pronounced effect than power capping. In both the medium- and high-energy regions, the most restrictive PTO damping capping led to increases in LCOE of 235% and 249% respectively.

It can therefore be concluded that limiting power production has a significant and adverse effect on the LCOE in wave energy, with capping the PTO damping coefficient having a substantially larger impact on the LCOE, for both medium- and high-energy regions, in comparison to power capping.

Discussion and Recommendations

Throughout this research, the main objective was to find the general influence of limiting power production on the LCOE. This lead to the choices of using regular waves, a constant PTO damping coefficient and two locations with different energy densities. As a result, the final numbers of AEP and LCOE/kg are slightly overestimated and inapplicable to real-life applications. It is therefore important to note that those absolute values are to be used for comparison. The percentage changes are more important and can act as a benchmark for optimization studies.

The results presented in this thesis resulted in understanding how limiting power production influences the LCOE for both medium- and high-energy regions. However, the scope of this research was limited to regular wave conditions and non-optimized power take-off (PTO) damping coefficients. To further explore the influence of capping on the LCOE, it would be valuable to extend the study to an optimization study. This could include irregular wave conditions and optimized PTO settings, moving away from the more general findings in this research. Investigating whether the trend of increasing LCOE with stricter capping parameters is similar under these conditions could provide deeper insights into real-world applications.

Further exploration into the mechanics of PTO systems is recommended as well. Comparing different types of PTO systems and examining their specific influence on the LCOE when subjected to capping could further explore this topic. It would be especially interesting to vary with the mass and size of PTO systems to compare the LCOE/kg between different options. Using this approach, not only the AEP, but the CAPEX and possibly the OPEX might change as well.

Additionally, the economic model used in this thesis employed average percentages to estimate CAPEX and OPEX, which provided a generalized result rather than a location-specific one. It is advised that optimization studies consider developing more tailored economic models that factor in location-specific costs such as local manufacturing capabilities, material costs and logistical considerations. This approach could potentially reveal opportunities for significant cost reductions, making wave energy projects more economically viable and providing more realistic values of LCOE/kg instead of the comparative values of this research.

References

[1] World Resources Institute. *4 Charts Explain Greenhouse Gas Emissions by Countries and Sectors*. 2023. URL: https://www.wri.org/insights/4-charts-explain-greenhouse-gas-emissions-countries-and-sectors#:~:text=The%20Energy%20Sector%20Produces%20the%20Most%20Greenhouse%20Gas%20Emissions&text=The%20energy%20sector%20includes%20transportation,emissions%20and%20other%20fuel%20combustion.

[2] European Commission. *Website Title*. URL: https://climate.ec.europa.eu/eu-action/climate-strategies-targets/2030-climate-targets_en (visited on 2024).

[3] Pukha Lenee-Bluhm, Robert Paasch, and H. Tuba Özkan-Haller. "Characterizing the wave energy resource of the US Pacific Northwest". In: *Renewable Energy* 36.8 (2011), pp. 2106–2119. ISSN: 0960-1481. DOI: https://doi.org/10.1016/j.renene.2011.01.016. URL: https://www.sciencedirect.com/science/article/pii/S0960148111000383.

[4] A. Al-Habaibeh, D. Su, J. McCague, and A. Knight. "An innovative approach for energy generation from waves". In: *Energy Conversion and Management* 51.8 (2010). Global Conference on Renewables and Energy Efficiency for Desert Regions (GCREEDER 2009), pp. 1664–1668. ISSN: 0196-8904. DOI: https://doi.org/10.1016/j.enconman.2009.11.041. URL: https://www.sciencedirect.com/science/article/pii/S0196890409004919.

[5] B Drew, A R Plummer, and M N Sahinkaya. "A review of wave energy converter technology". In: *Proceedings of the Institution of Mechanical Engineers, Part A: Journal of Power and Energy* 223.8 (2009), pp. 887–902. DOI: 10.1243/09576509JPE782. URL: https://doi.org/10.1243/09576509JPE782.

[6] A. de Andres, R. Guanche, C. Vidal, and I.J. Losada. "Adaptability of a generic wave energy converter to different climate conditions". In: *Renewable Energy* 78 (2015), pp. 322–333. ISSN: 0960-1481. DOI: https://doi.org/10.1016/j.renene.2015.01.020. URL: https://www.sciencedirect.com/science/article/pii/S0960148115000270.

[7] Iraide López, Jon Andreu, Salvador Ceballos, Iñigo Martínez De Alegría, and Iñigo Kortabarria. "Review of wave energy technologies and the necessary power-equipment". In: *Renewable and sustainable energy reviews* 27 (2013), pp. 413–434.

[8] Dave Levitan. "Why Wave Power Has Lagged Far Behind as Energy Source". In: *Yale E360* (2014). URL: https://e360.yale.edu/features/why_wave_power_has_lagged_far_behind_as_energy_source.

[9] World Economic Forum. "Wave energy: can ocean power solve the global energy crisis?" In: (2021). URL: https://www.weforum.org/agenda/2021/09/wave-energy-potential-challenges/.

[10] International Renewable Energy Agency. *Wave Energy: Technology Brief*. Tech. rep. IRENA, 2014. URL: https://www.irena.org/-/media/Files/IRENA/Agency/Publication/2014/Wave-Energy_V4_web.pdf.

[11] Elena Baca, Ritu Treisa Philip, David Greene, and Hoyt Battey. *Expert elicitation for wave energy lcoe futures*. Tech. rep. National Renewable Energy Lab.(NREL), Golden, CO (United States), 2022.

[12] Chenglong Guo, Wanan Sheng, Dakshina G De Silva, and George Aggidis. "A review of the levelized cost of wave energy based on a techno-economic model". In: *Energies* 16.5 (2023), p. 2144.

[13] Adrian De Andres, Jéromine Maillet, Jørgen Hals Todalshaug, Patrik Möller, David Bould, and Henry Jeffrey. "Techno-Economic Related Metrics for a Wave Energy Converters Feasibility Assessment". In: *Sustainability* 8.11 (2016). ISSN: 2071-1050. DOI: 10.3390/su8111109. URL: https://www.mdpi.com/2071-1050/8/11/1109.

[14] Jian Tan, Henk Polinder, Antonio Jarquin Laguna, Peter Wellens, and Sape A. Miedema. "The Influence of Sizing of Wave Energy Converters on the Techno-Economic Performance". In: *Journal of Marine Science and Engineering* 9.1 (2021). ISSN: 2077-1312. DOI: 10.3390/jmse9010052. URL: https://www.mdpi.com/2077-1312/9/1/52.

[15] Eugen Rusu and Florin Onea. "Wave Energy Evaluations in Enclosed Seas". In: Jan. 2012.

[16] Alexis Merigaud and John Ringwood. "Power production assessment for wave energy converters: Overcoming the perils of the power matrix". In: *Proceedings of the Institution of Mechanical Engineers, Part M: Journal of Engineering for the Maritime Environment* 232 (Feb. 2018), pp. 50–70. DOI: 10.1177/1475090217731671.

[17] A. Babarit, J. Hals, M.J. Muliawan, A. Kurniawan, T. Moan, and J. Krokstad. "Numerical benchmarking study of a selection of wave energy converters". In: *Renewable Energy* 41 (2012), pp. 44–63. ISSN: 0960-1481. DOI: https://doi.org/10.1016/j.renene.2011.10.002. URL: https://www.sciencedirect.com/science/article/pii/S0960148111005672.

[18] Raju Ahamed, Kristoffer Mckee, and Ian Howard. "Advancements of wave energy converters based on power take off (PTO) systems: A review". In: *Ocean Engineering* 204 (May 2020), p. 107248. DOI: 10.1016/j.oceaneng.2020.107248.

[19] Shuang Wu, Yanjun Liu, and Jian Qin. "Experimental analyses of two-body wave energy converters with hydraulic power take-off damping in regular and irregular waves". In: *IET Renewable Power Generation* 15 (June 2021). DOI: 10.1049/rpg2.12218.

[20] Bingyong Guo, Tianyao Wang, Siya Jin, Shunli Duan, Kunde Yang, and Yaming Zhao. "A Review of Point Absorber Wave Energy Converters". In: *Journal of Marine Science and Engineering* 10.10 (2022). ISSN: 2077-1312. DOI: 10.3390/jmse10101534. URL: https://www.mdpi.com/2077-1312/10/10/1534.

[21] Tunde Aderinto and Hua Li. "Review on Power Performance and Efficiency of Wave Energy Converters". In: *Energies* 12.22 (2019). ISSN: 1996-1073. DOI: 10.3390/en12224329. URL: https://www.mdpi.com/1996-1073/12/22/4329.

[22] António FO Falcão and Joao CC Henriques. "Oscillating-water-column wave energy converters and air turbines: A review". In: *Renewable energy* 85 (2016), pp. 1391–1424.

[23] Erlantz Otaola, Aitor Garrido, Jon Lekube, and Izaskun Garrido. "A Comparative Analysis of Self-Rectifying Turbines for the Mutriku Oscillating Water Column Energy Plant". In: *Complexity* 2019 (Jan. 2019), pp. 1–14. DOI: 10.1155/2019/6396904.

[24] Ocean Energy. *Ocean Energy Buoy*. 2024. URL: https://oceanenergy.ie/oe-buoy/.

[25] Robert Mayon, Dezhi Ning, Boyin Ding, and Nataliia Sergiienko. "Wave energy converter systems – status and perspectives". In: July 2022, pp. 3–58. ISBN: 9781003198956. DOI: 10.1201/9781003198956-1.

[26] CorPower Ocean. *"CorPower Ocean Unveils Commercial Scale Products to Unleash Utility Scale Wave Farms"*. 2024. URL: https://corpowerocean.com/corpower-ocean-unveils-commercial-scale-products-to-unleash-utility-scale-wave-farms/#:~:text=The%20CorPower%20C4%2C%20with%20300kW,produced%20rapidly%20in%20large%20volumes..

[27] *CorPower C4 WEC*. https://www.innoenergy.com/discover-innovative-solutions/online-marketplace-for-energy-innovations/corpower-c4/. Accessed: 2024-07-18.

[28] European Marine Energy Centre. *Pelamis Wave Power*. 2024. URL: https://www.emec.org.uk/about-us/wave-clients/pelamis-wave-power/.

[29] Tethys, Pacific Northwest National Laboratory. *Wave Dragon Pre-Commercial Demonstration Project*. 2024. URL: https://tethys.pnnl.gov/project-sites/wave-dragon-pre-commercial-demonstration-project.

[30] J.N. Reddy. "Numerical Methods, Finite Element". In: *Encyclopedia of Solid Earth Geophysics*. Ed. by H.K. Gupta. Springer, Dordrecht, 2011, pp. 892–895. DOI: 10.1007/978-90-481-8702-7_37. URL: https://link.springer.com/referenceworkentry/10.1007/978-90-481-8702-7_37.

[31] D.E. Beskos. "Boundary Element Methods in Structural Analysis". In: *Boundary Elements XVIII*. WIT Press, 1996, pp. 201–210. URL: https://www.witpress.com/Secure/elibrary/papers/BE96/BE96019FU.pdf.

[32] Yingyi Liu. "HAMS: A Frequency-Domain Preprocessor for Wave-Structure Interactions—Theory, Development, and Application". In: *Journal of Marine Science and Engineering* 7.3 (2019). ISSN: 2077-1312. DOI: 10.3390/jmse7030081. URL: https://www.mdpi.com/2077-1312/7/3/81.

[33] Matt Folley. *Numerical modelling of wave energy converters: state-of-the-art techniques for single devices and arrays*. Academic Press, 2016.

[34] Edgard Malta, Rodolfo Gonçalves, Fabio Matsumoto, Felipe Rateiro, André Fujarra, and Kazuo Nishimoto. "Damping Coefficient Analyses for Floating Offshore Structures". In: June 2010. DOI: 10.1115/OMAE2010-20093.

[35] Guido M Terra, Willem Jan van de Berg, and Leo R M Maas. "Experimental verification of Lorentz' linearization procedure for quadratic friction". In: *Fluid Dynamics Research* 36.3 (2005), p. 175. DOI: 10.1016/j.fluiddyn.2005.01.005. URL: https://dx.doi.org/10.1016/j.fluiddyn.2005.01.005.

[36] Jos van 't Hoff, Matt Folley, and Trevor Whittaker. "The design of small seabed-mounted bottom-hinged wave energy converters". In: Sept. 2007.

[37] M. Folley and T. Whittaker. "Spectral modelling of wave energy converters". In: *Coastal Engineering* 57.10 (2010), pp. 892–897. ISSN: 0378-3839. DOI: https://doi.org/10.1016/j.coastaleng.2010.05.007. URL: https://www.sciencedirect.com/science/article/pii/S0378383910000700.

[38] Jørgen Hals Todalshaug, Gunnar Steinn Ásgeirsson, Eysteinn Hjálmarsson, Jéromine Maillet, Patrik Möller, Pedro Pires, Matthieu Guérinel, and Miguel Lopes. "Tank testing of an inherently phase-controlled wave energy converter". In: *International Journal of Marine Energy* 15 (2016). Selected Papers from the European Wave and Tidal Energy Conference 2015, Nante, France, pp. 68–84. ISSN: 2214-1669. DOI: https://doi.org/10.1016/j.ijome.2016.04.007. URL: https://www.sciencedirect.com/science/article/pii/S2214166916300182.

[39] Xinyuan Shao, Uday Rajdeep Sakleshpur Lokesh Gowda, Hrishikesh Nitin Khedkar, Jørgen Hals Todalshaug, Jonas W Ringsberg, and Hua-Dong Yao. "Sensitivity Study of the Array Design for a Bottom-Fixed Heaving Point Absorber Wec". In: *Hrishikesh Nitin and Hals Todalshaug, Jørgen and Ringsberg, Jonas W. and Yao, Hua-Dong, Sensitivity Study of the Array Design for a Bottom-Fixed Heaving Point Absorber Wec* (2023).

[40] Subrata Kumar Chakrabarti. *Offshore structure modeling*. Vol. 9. world scientific, 1994.

[41] Jorgen Hals, Torkel Bjarte-Larsson, and Johannes Falnes. "Optimum reactive control and control by latching of a wave-absorbing semisubmerged heaving sphere". In: *International Conference on Offshore Mechanics and Arctic Engineering*. Vol. 36142. 2002, pp. 415–423.

[42] Zhe Ma, Yanjun Mao, Yong Cheng, and Gangjun Zhai. "Effect of the PTO Damping Force on the 2D Oscillating Buoy Wave Energy Converter Integrated into a Pile-Restrained Floating Breakwater". In: *Iranian Journal of Science and Technology, Transactions of Mechanical Engineering* 44 (2020), pp. 961–973.

[43] BEMRosetta Development Team. *BEMRosetta: Boundary Element Method for Wave-Structure Interaction Analysis*. https://github.com/BEMRosetta/BEMRosetta. 2024.

[44] Matias Alday, Vaibhav Raghavan, and George Lavidas. "Analysis of the North Atlantic offshore energy flux from different reanalysis and hindcasts". In: *Proceedings of the European Wave and Tidal Energy Conference*. Vol. 15. 2023.

[45] George Lavidas and Vengatesan Venugopal. “Characterising the wave power potential of the Scottish coastal environment”. In: *International Journal of Sustainable Energy* 37.7 (2017), pp. 684–703. DOI: 10.1080/14786451.2017.1347172.

[46] A. de Andres, E. Medina-Lopez, D. Crooks, O. Roberts, and H. Jeffrey. “On the reversed LCOE calculation: Design constraints for wave energy commercialization”. In: *International Journal of Marine Energy* 18 (2017), pp. 88–108. ISSN: 2214-1669. DOI: https://doi.org/10.1016/j.ijome.2017.03.008. URL: https://www.sciencedirect.com/science/article/pii/S2214166917300334.

[47] Jian Tan, Xuezhou Wang, Henk Polinder, Antonio Jarquin Laguna, and Sape A. Miedema. “Downsizing the Linear PM Generator in Wave Energy Conversion for Improved Economic Feasibility”. In: *Journal of Marine Science and Engineering* 10.9 (2022). ISSN: 2077-1312. DOI: 10.3390/jmse10091316. URL: https://www.mdpi.com/2077-1312/10/9/1316.

[48] Marianna Giassi, Valeria Castellucci, and Malin Göteman. “Economical layout optimization of wave energy parks clustered in electrical subsystems”. In: *Applied Ocean Research* 101 (2020), p. 102274. ISSN: 0141-1187. DOI: https://doi.org/10.1016/j.apor.2020.102274. URL: https://www.sciencedirect.com/science/article/pii/S0141118720300869.

[49] Malin Göteman, Cameron McNatt, Marianna Giassi, Jens Engström, and Jan Isberg. “Arrays of Point-Absorbing Wave Energy Converters in Short-Crested Irregular Waves”. In: *Energies* 11.4 (2018). ISSN: 1996-1073. DOI: 10.3390/en11040964. URL: https://www.mdpi.com/1996-1073/11/4/964.

[50] Pinar Tokat and Torbjörn Thiringer. “Sizing of IPM Generator for a Single Point Absorber Type Wave Energy Converter”. In: *IEEE Transactions on Energy Conversion* 33.1 (2018), pp. 10–19. DOI: 10.1109/TEC.2017.2741582.

[51] *Eurozone Historical Inflation Rates | 1991-2024*. Accessed: June 7, 2024. 2024. URL: https://www.inflationtool.com/eurozone/historical-inflation-rates.

[52] *Inflation in the euro area - Statistics Explained*. Accessed: June 7, 2024. 2024. URL: https://ec.europa.eu/eurostat/statistics-explained/index.php?title=Inflation_in_the_euro_area.

[53] World Economic Forum. *How could inflation change in the Eurozone for 2023?* Accessed: June 7, 2024. 2023. URL: https://www.weforum.org/agenda/2023/01/eurozone-inflation-outlook-2023.

[54] R. Guanche, A.D. de Andrés, P.D. Simal, C. Vidal, and I.J. Losada. “Uncertainty analysis of wave energy farms financial indicators”. In: *Renewable Energy* 68 (2014), pp. 570–580. ISSN: 0960-1481. DOI: https://doi.org/10.1016/j.renene.2014.02.046. URL: https://www.sciencedirect.com/science/article/pii/S0960148114001372.

[55] George Lavidas and Kornelis Blok. “Levelised Cost of Electricity for wave energy converters and the perception of milder resource non-viability in the North Sea”. In: *Proceedings of the 14th European Wave and Tidal Energy Conference*. 2021.